

The Pennsylvania State University

The Graduate School

College of Engineering

**MICROWAVE IMAGING SYSTEM DEVELOPMENT FOR NONDESTRUCTIVE
TESTING OF MULTILAYER STRUCTURES USING ULTRAWIDEBAND NOISE
WAVEFORMS**

A Thesis in

Electrical Engineering

by

Marc D. Navagato

© 2018 Marc D. Navagato

Submitted in Partial Fulfillment
of the Requirements
for the Degree of

Master of Science

August 2018

The thesis of Marc D. Navagato was reviewed and approved* by the following:

Ram M. Narayanan
Professor of Electrical Engineering
Thesis Advisor

Julio V. Urbina
Associate Professor of Electrical Engineering

Kultegin Aydin
Professor of Electrical Engineering
Head of the Department of Electrical Engineering

*Signatures are on file in the Graduate School

ABSTRACT

Many areas within the aerospace, automotive, civil, and consumer industries rely on the superior structural support and lightweight characteristics of composite materials. These composites are used heavily in military applications, where they are applied extensively to the interior and exteriors of various aircrafts, ships, and land vehicles. The problem, though, is that during the lifespan of these composite materials, they are subject to various hazards, such as impact damages and galvanic corrosion, which may cause significant physical damage and financial costs.

Our research is conducted with the goal of identifying potential flaws within the internal layers of such composite materials using ultrawideband noise waveforms. Noise and pseudorandom noise waveforms foster many benefits over other traditional waveforms due to their excellent resolution capabilities, low-probability of intercept, and immunity to jamming characteristics.

The system we have designed, which operates in the X-band frequency range (8.2-12.4 GHz), scans a sample within the near-field of a pair of aperture horn antennas and creates either a two-dimensional or three-dimensional reconstructed image of the sample under test. We have developed samples with traits similar to those of composites that have experienced real-world damages or defects. Our findings have allowed for the detection of air voids in glass-fiber reinforced polymer civil structures; detection of aluminum hydroxide ($\text{Al}(\text{OH})_3$)—a byproduct of galvanic corrosion—in hybrid composite materials; as well internal ply delaminations in unidirectional carbon-fiber reinforced polymers due to high mass, low velocity tool drops.

TABLE OF CONTENTS

List of Figures.....	vi
List of Tables.....	x
Acknowledgments.....	xi
Chapter 1 Introduction	1
1.1 Introduction to Non-Destructive Testing (& Evaluation)	1
1.2 Introduction to Composite Materials	2
1.2.1 Damages within Fiber-Reinforced Polymer Strengthened Materials	3
1.2.2 Synthetic Galvanic Corrosion in Hybrid Composite Materials	6
1.3 Ultrawideband Noise Radar Systems and Microwave Imaging.....	7
Chapter 2 Fundamentals	10
2.1 Electromagnetic characteristics of Multilayered Materials.....	10
2.2 Operational Fundamental of Radar Systems.....	15
2.2.1 Theoretical Range Resolution.....	16
2.2.2 Signal-to-Noise Ratio of Systems	17
2.2.3 Matched Filtering via Digital Cross-Correlation	20
2.2.4 Coherent Pulse Integration.....	22
Chapter 3 Waveforms for NDT Microwave Imaging	28
3.1 Ultrawideband Waveforms	28
3.1.1 Linear Frequency Modulated Chirp Waveforms	28
3.1.2 Gaussian-Modulated Sinusoidal Pulses	29
3.1.3 Pseudorandom Noise Pulses	31
3.2 Waveform Performances.....	35
Chapter 4 NDT Microwave Imaging System Design and Performance	38
4.1 RF Component Descriptions	38
4.1.1 Voltage-Controlled Oscillators	38
4.1.2 Frequency Conversion Mixers	40
4.1.3 RF Amplifiers	43
4.1.4 UWB Horn Antennas	44
4.2 System Description and Performance	47
4.2.1 System RF Front End.....	49
Chapter 5 System Validation and Experimental Results	57
5.1 Testing Requirements for Near-Field Imaging	59

5.1.1	Standoff distance Optimization Method	59
5.1.2	Sampling Coherence of Reflected Data	61
5.2	System Validation Measurements.....	61
5.2.1	A-Scan Target Ranging Tests of Cylindrical PEC Targets.....	61
5.2.2	B-scans of Single and Multiple Cylindrical Objects.....	63
5.2.3	C-scans of Polyvinyl Chloride (PVC) Sample with Water Inclusion	66
5.3	Composite Material Experiments.....	72
5.3.1	GFRP Reinforced Cement Hybrid Wall with Air Void	72
5.3.2	Galvanic Corrosion of CFRP/Aluminum Hybrid Composite	75
5.3.3	Impact Damaged CFRP Sample	78
Chapter 6 Conclusion and Suggestions for Future Work		81
6.1	Conclusions.....	81
6.2	Future Work.....	82
References.....		83
Appendix A.....		89
CFRP Sample Preparation and Safety Procedures.....		89
Appendix B.....		92
Transducer Gain.....		92
Appendix C.....		94
FIR Filters		94

LIST OF FIGURES

Figure 1-1 (a) F-22 construction is of 24% composite material (Source: https://www.airforce-technology.com/projects/f22/). (b) Airbus A350 XWB construction is of 50% composite material (Source: http://www.airbus.com/newsroom/press-releases/en/2016/10/airbus-a350-xwb-starts-its-china-tour-with-debut-at-zhuhai-airshow.html)	3
Figure 1-2: Layup techniques for CFRP composite materials (Source: https://www.quartus.com/resources/composites-101/)	4
Figure 1-3: High mass, low velocity impact from tool	4
Figure 1-4: Low velocity impact damage (Source: [10]).....	5
Figure 1-5: Illustration of galvanic corrosion between a hybrid composite configuration of aluminum and CFRP.....	7
Figure 2-1: Normal EM wave propagation through a N -layered multilayer material (adapted from [26])	13
Figure 2-2: (a) Model of CFRP without and with internal delaminations and (b) calculated reflection coefficient (application of equation 2.13) for each case.	14
Figure 2-3: Available antenna configurations: (a) Monostatic, (b) bistatic, (c) multistatic, and (d) pseudo-monostatic	15
Figure 2-4: Comparisons of SNRs and NFs of radar receivers without (a & b) and with (c & d) a LNA with low noise factor after the receiving antenna.	19
Figure 2-5: Autocorrelation output of noise sequence.....	21
Figure 2-6: Comparisons of the spectral content of the raw radar data (red trace) and the cross-spectral data of output of the cross-correlation operation (blue trace). Applying the matched filter significantly increases the overall SNR of the radar receiver.	22
Figure 2-7: Benefits of coherent pulse integration. SNR of white-noise signal corrupted with external noise increased after integration of 50 pulses	24
Figure 2-8: Simulated transmitted pulse and reflected pulses from two closely separate scatterers.....	25
Figure 2-9: Matched filter output for 0 dB SNR on receive, shown for 5, 30, and 60 coherent pulse integrations.....	26
Figure 2-10: Matched filter output for 10 dB SNR on receive, shown for 5, 30, and 60 coherent pulse integrations.....	26

Figure 2-11: Matched filter output for 20 dB SNR on receive, shown for 5, 30, and 60 coherent pulse integrations.....	27
Figure 3-1: Time and frequency domain representation of LFM chirp pulse.....	29
Figure 3-2: Comparisons of time and frequency domains of standard Gaussian pulses (a) and (b) and sinusoidal-modulated Gaussian pulses (c) and (d), for different values of σ	31
Figure 3-3: Time and frequency domain representations of application of equation (3) (a&b) and of equation (4) (c&d) for 1000 ($N = 1000$) separate sinusoids of random frequency and phase.....	33
Figure 3-4: Alternate noise pulse generation method in the time-domain (a) along with the corresponding frequency spectrum (b).....	34
Figure 3-5: Histogram using of amplitudes of 250 noise signals measured at 1.5 ns while generating noise pulses using equation 8 (a) and while using a random number generator to assign amplitude values (b).....	34
Figure 3-6: (Top row) Chirp signals for $\beta\tau = 10$, $\beta\tau = 25$ and $\beta\tau = 100$ and their frequency domain representations (bottom row)	35
Figure 3-7: Simulated range profiles of scene with two targets separated by 6 cm while using a noise pulse with a high PSLR (a) and noise pulse with a low PSLR (b).....	36
Figure 3-8: PSLR distribution for 1000 iterations of Gaussian noise pulses with a bandwidth of 4 GHz. The dashed/dotted blue line represents the PSLR of a chirp of equal bandwidth and the dashed red line corresponds to the PSLR of a sinusoidal-modulated Gaussian pulse, also of equal bandwidth.....	37
Figure 4-1: Block diagram of oscillator feedback network	39
Figure 4-2: Frequency up-conversion using a mixer. (a) functional diagram (b) time-domain plots of each signal component and (c) associated spectral components of the up-conversion process.....	41
Figure 4-3: Frequency down-conversion using a mixer. (a) functional diagram (b) time-domain plots of each signal component and (c) associated spectral components of the down-conversion process.....	42
Figure 4-4: Amplifier gain characteristics (measured and supplied from manufacturer), listed as maintaining a high gain and flat response of $24 \text{ dB} \pm 1.3 \text{ dB typ}$, over X-band frequency range	44
Figure 4-5: (a) One of two actual horn antennas used for NDT microwave imaging and (b) FEKO [®] simulation model.....	45
Figure 4-6: Near field simulation results of horn antenna in Figure 4-5	46

Figure 4-7: X-band microwave imaging radar system block diagram.....	47
Figure 4-8: Complete NDT microwave imaging system	48
Figure 4-9: RF front-end (a) connection panel and (b) component layout views	50
Figure 4-10: Simulink simulation of up-conversion block.	51
Figure 4-11: Simulation results of the upconversion chain of the RF front end: (a) Transducer gain, (b) SNR and, (c) noise factor.....	52
Figure 4-12: Simulink simulation of downconverter block.	53
Figure 4-13: Simulation results of the downconversion chain of the RF front end: (a) Transducer gain, (b) SNR and, (c) noise factor.....	54
Figure 4-14: Simulink simulation of reference channel block.....	55
Figure 4-15: Block diagram of LO conditioning channel used for mixing stages, with noise figures and amplifier non-linearities accounted for.....	56
Figure 4-16: Simulated output of LO channel.	56
Figure 5-1: Range optimization tests for CFRP panel. (a) Raw voltage peak-to-peak data for cases of with and without target behind sample and (b) the voltage differences at each range.	60
Figure 5-2: Measurement setup for range-resolution validation tests.....	62
Figure 5-3: Range profiles of two cylindrical PEC targets separated by (a) 20 cm (b) 10 cm (c) 3.75 cm and (d) 2.5 cm.	63
Figure 5-4: System coordinates for 2-D scan.....	64
Figure 5-5: (a-c) Scanning path of antennas for B-scan of single cylindrical PEC target and (d) results.....	65
Figure 5-6: B-scan results of 3 targets (wooden rod and two cylindrical PECs).....	66
Figure 5-7: Data organization scheme (for arbitrary 5×5×6 set of data), where colored boxes represents data gathered at one sampling location or a single A-scan.....	67
Figure 5-8: (a) Water inclusion placed in cavity (b) of PVC sample.....	67
Figure 5-9: Measurement geometry of PVC sample with hidden water inclusion between layers.	68
Figure 5-10: Antenna orientation with respect to PVC sample with hidden water inclusion..	68

Figure 5-11: Geometry which shows range definition and orientation of slices for viewing 3 dimensional data sets.	69
Figure 5-12: C-scan results a PVC sample using GMSP	70
Figure 5-13: C-scan results a PVC sample using noise pulse with high PSLR	71
Figure 5-14: C-scan results a PVC sample using noise pulse with low PSLR	71
Figure 5-15: Concrete wall before adhering GFRP panel. (a) Shaded region represents area where no adhesion is to be applied, which results in air gap between concrete and GFRP boundary. (b) Completed concrete/GFRP wall in place for C-scan trials, with the white outline representing location of air void (bonding defect).	72
Figure 5-16: Measurement setup for detection of air void in GFRP/concrete wall structure.....	73
Figure 5-17: C-scan results of GFRP/cement wall hybrid using (a) GMSP and using (b) noise pulse.....	74
Figure 5-18: Sample preparation for corrosion measurement tests. (a) Laboratory grade $\text{Al}(\text{OH})_3$ powder (b) Metal backing plate with cavity and $\text{Al}(\text{OH})_3$ sample; (c) CFRP panel coupled to front of metal backing plate.	75
Figure 5-19: Scan results of CFRP/aluminum hybrid sample (a) without the presence of $\text{Al}(\text{OH})_3$ and (b) with $\text{Al}(\text{OH})_3$ present.	77
Figure 5-20: Hammer used from impact damage testing of CFRP panel.	78
Figure 5-21: (a) CFRP panel with impact damage from hammer. Location of impact denoted by “X”. (b) Close-up of location of impact, showing minor surface cracking. ...	79
Figure 5-22: C-scan results of impact damage due to hammer drop on CFRP composite sample	80

LIST OF TABLES

Table 5-1: Summary of Testing Variables.....	58
Table 5-2: Constant System Parameters.....	58
Table 5-3: Parameters for Multilayer PVC Sample with Water Inclusion C-scans.....	69
Table 5-4: Parameters for GFRP/Cement Hybrid Wall C-scans.....	73
Table 5-5: Parameters for CFRP/Aluminum Hybrid Composite with Al(OH) ₃ C-scans.....	76
Table 5-6: Parameters for CFRP Composite with Impact Damage.....	79

ACKNOWLEDGEMENTS

I would like to thank all my fellow researchers in the Radar and Communications Lab for their support and insight into a wide array of topics covered during all the stages of my research. I would like to personally thank Tae Hee Kim, Robin James, and Sean Kaiser for their help with establishing foundational concepts for this work and in the development of the imaging system. Many thanks must be made to my advisor Dr. Ram Narayanan and committee member Dr. Julio Urbina for all of the support, patience, and guidance they gave me during my research—it was, and still is incredibly appreciated.

Finally, I would also like to thank William Nickerson of the Office of Naval Research (ONR) for supporting our research under grant/contract number N00014-15-1-2021.

The findings and conclusions presented herein do not necessarily reflect the view of the funding agency.

DEDICATION

For all their loving support, words of encouragement, and belief in me during my academic journey, I dedicate this thesis to my parents, stepparents, and soon-to-be parents-in-law, Carol, Pat, Paula, Rick, Doreen and Doug, as well as all my friends and family.

Also, to my soon-to-be wife, Chelsea, your belief in me is what gave me the inspiration to work so hard and what continues to motivate me every day.

Chapter 1 Introduction

1.1 Introduction to Non-Destructive Testing (& Evaluation)

Dating back to as early as the 1950's, non-destructive testing (NDT) techniques have been used to determine the state of various structures, materials, and systems. It is an approach where the internal composition of a material may be interrogated without, in some cases, making physical contact or requiring a coupling agent [1]. This ability serves as a great importance in the early detection of flaws within the skins of military assets and commercial structures. It is of great interest to develop a low-cost method of detecting these flaws before catastrophic failures occur.

Most common current methods of NDT consist of: visual inspection; radiographic examination using X-ray radiation; ultrasonic testing using high-frequency sound waves; magnetic particle inspection (MPI) using iron particles; liquid penetrant testing; and electromagnetic methods consisting of eddy-current testing and microwave imaging. Of these approaches, visual inspection is the most common and is used in nearly 80 percent of NDT applications. This approach primarily only allows for detection of significant physical damage, misalignment of parts, weathering, surface blemishes and non-uniformities [2, 3]. Many of the aforementioned methods come at either at a high cost high or high degree of invasiveness, which makes microwave imaging systems more attractive in many cases.

The microwave imaging approach uses the reflection and transmission of electromagnetic (EM) pulses, which occur between boundaries within a material, to learn about the condition of the internal structure of a sample. This leads to the ability of revealing hidden inclusions, deformations, and presence of air voids, as microwave signals are able to penetrating within the layers of various

dielectrics. Additionally, typical microwave imaging systems operate under low power restrictions, proving great benefits to NDT [4].

The limitations of NDT microwave imaging lie in both the constitutive parameters and dimensions of the dielectric material under test (MUT)—as well as the signal that is incident upon it. The amount of attenuation an EM wave experiences is mainly based on the materials ability to absorb microwave energy at certain frequencies [1]. Therefore designing a NDT radar system with an abundance of frequency content will increase the likelihood of detection of these minute flaws.

1.2 Introduction to Composite Materials

Known for their superior strength and relative lightness, composite materials have made their everlasting footprint in the aerospace industry as one of the leading materials used in the construction of landing gears, doors, winglets, fins, and trailing edges—just to name a few. Composite materials are widely used in the ubiquitous F-22, shown in Figure 1-1a, and also in commercial aircrafts such as the Airbus A350 XWB, shown in Figure 1-1b, which boasts a 25 % increase in fuel efficiency due to its greater than 50 % composition of composite materials [5]. They have also been used in many civil applications for reinforcements of bridges and walls.

The strength of these materials comes due to the conjunction of fibrous materials such as carbon or glass with a strong bonding resin such as epoxy. The variations in the individual properties, when put together, are what create a much stronger composite sample.



(a)

(b)

Figure 1-1 (a) F-22 construction is of 24% composite material (Source: <https://www.airforce-technology.com/projects/f22/>). (b) Airbus A350 XWB construction is of 50% composite material (Source: <http://www.airbus.com/newsroom/press-releases/en/2016/10/airbus-a350-xwb-starts-its-china-tour-with-debut-at-zhuhai-airshow.html>).

1.2.1 Damages within Fiber-Reinforced Polymer Strengthened Materials

During the lifespan of a composite material, degradations due to continuous use and exposure to impact damages may cause serious structural and internal damage. In many cases, these damages are localized to the internal structure of the composite material and are not visible to the human eye. Various studies [6, 7, 8, 9] have investigated the use of near-field microwave inspection methods for detection of disbonds within fiber-reinforced polymer (FRP) materials due to impact damages from hail stones (low mass, high velocity), runway debris (low mass, high velocity), dropped tools (high mass, low velocity), bird strikes (low mass, high velocity), presence of moisture, and poor applications of laminate bonding materials.

A very common type of FRP is the carbon-fiber reinforced polymer (CFRP), which is commonly used as skins of aircrafts, marine equipment, and structural support in civil applications. CFRP composites are comprised of multiple carbon fiber loaded plies stacked on top of each other in either a unidirectional or quasi-isotropic fashion, as shown in Figure 1-2.

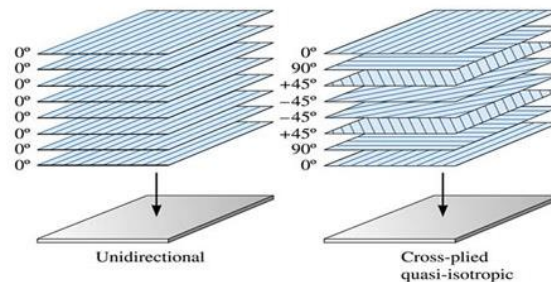


Figure 1-2: Layup techniques for CFRP composite materials (Source: <https://www.quartus.com/resources/composites-101/>).

CFRP exhibits superior structural strength and stiffness, but when subjected to impact damages, cracking and delamination within the inner plies of a sample may occur. An example of a high mass, low velocity tool drop impact (12 J of energy upon impact) on an 8-ply unidirectional CFRP sample is shown in Figure 1-3. The impact took place under a no-load condition and shows

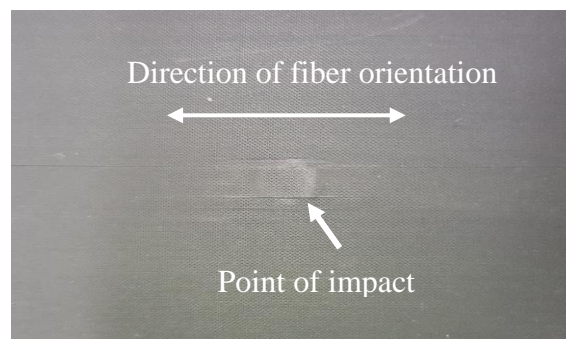


Figure 1-3: High mass, low velocity impact from tool (12 J of energy) on unidirectional CFRP.

visible surface damage, as well as ply delamination in the direction of the conductive carbon fibers. This is an extreme case where the damage is visible to the human eye, but in many scenarios, when the energy upon impact is considerably less, internal cracking and delaminations are not visible to the human eye. Figure 1-4 shows a high-resolution photograph of internal damages within a 16-ply CFRP composite sample that would not be visible to the human eye. When a composite experiences delamination, as shown in Figure 1-4, microwave imaging approaches are able to detect these flaws.

Since CFRP composites are based on multiple unidirectional or quasi-isotropic ply layups, consisting of closely grouped highly conductive carbon fibers, electromagnetic (EM) energy is only able to penetrate into the internal ply layers based on the orientation of the electric field in comparison to the fibers. That is, for a multi-ply unidirectional sample, EM waves will only penetrate CFRPs when the electric field orientation is orthogonal to the direction of the carbon fibers. While in the case of a quasi-isotropic (the fibers of each ply are oriented at a different angles from each other) CFRP sample, EM energy is only capable of penetrating the outermost layers of the sample, as the fibers within deeper plies are aligned with the electric field, and have a high conductivity which tend to completely reflect the incident field. Alternatively, another type of composite material known as glass-fiber reinforced polymer (GFRP) has been proven to show

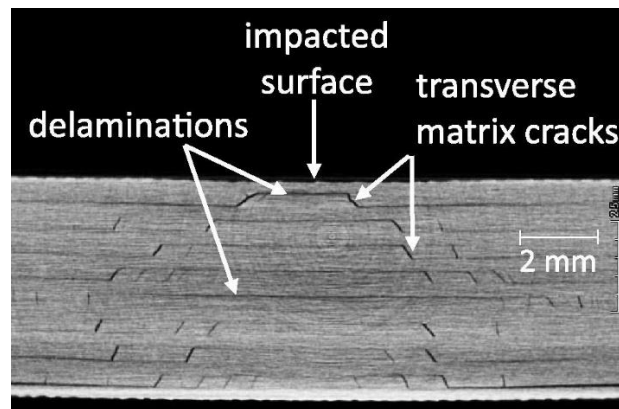


Figure 1-4: Low velocity impact damage (Source: [10]).

substantial resistance to impact loading [11]. Unlike CFRP, GFRP does not contain conductive fibers, but rather glass fibers, which allow EM energy to penetrate efficiently and at many, if not all, orientations of the electric field.

1.2.2 Synthetic Galvanic Corrosion in Hybrid Composite Materials

FRP composite materials, of many varieties, have been used in demanding automotive, aerospace, and marine application based environments, where they are coupled to metal materials to increase their fatigue and/or impact resistant properties [12]. Work conducted by Kim et al. uses aluminum/CFRP hybrid materials for use in the hull of an autonomous surface vehicle, which could be used for reconnaissance, anti-surface warfare, anti-underwater warfare, and mine detection missions. In most cases, aircraft skin linings are also made using this same hybrid method of coupling an FRP composite material directly to a metal surface.

The issue with this approach (as seen in aircrafts) is that when the doors of the aircrafts are opened—on land or on a carrier at sea—the plane fills with warm moist air. As the plane takes flight and becomes cold again, the moisture inside begins to condense and gathers inside the skin of the aircraft [2]. The issue then, in both sea and air based applications, is that any water containing a high degree of chlorides, Cl^- , acts as an ionizing electrolyte that reacts when in contact with a metal, causing a corrosion process to occur; this is once the protective oxide film of the aluminum deteriorates, due to chemical or mechanical damages [13].

When two metals, or any conductive materials, come in contact with each other and are exposed to an electrolyte such as rain or ocean spray, the process known as *galvanic corrosion* begins, as depicted in Figure 1-5. Under these conditions, the coupled metals tend to gain an electric potential known as a *corrosion potential*, where the metal which contains the most negative potential is known as the anode and the metal with the most positive charge is known as the cathode.

Typically, when the hybrid material is comprised of a CFRP/aluminum coupling, the aluminum acts as the anode and the CFRP acts as the cathode. When a potential differential exists between these metals, a current will flow from the cathode to the anode, which then causes the onset of corrosion on the anodic material, which is rightfully then known as the *sacrificial anode* [14].

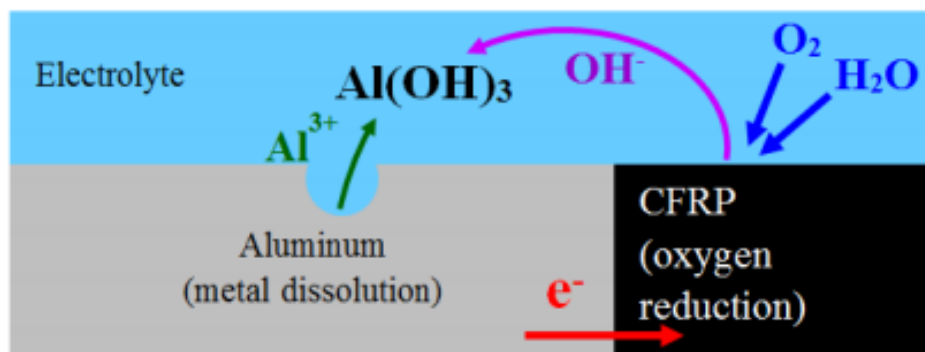


Figure 1-5: Illustration of galvanic corrosion between a hybrid composite configuration of aluminum and CFRP.

1.3 Ultrawideband Noise Radar Systems and Microwave Imaging

Similar to classical radar systems, noise radar systems are multifunctional in that they have many diverse applications, depending on the specific design. Such radars system have designed for through-wall radar imaging (TWRI) [15, 16, 17], synthetic aperture radar (SAR) imaging [18], target detection [19], and tomography applications [20], to list just a few. The original pioneer in noise radar was Richard Bourret who published the first paper on noise radar in 1957 [21], followed by B.M Horton who published a paper in 1959 discussing range measurements using noise waveforms [22].

A type of waveform where the bandwidth of the signal (frequency ranges covered) exceeds 20% of the center frequency is known as *ultrawideband* (UWB) waveform. UWB signal generation has been a main area of waveform development dating back to research conducted by Heinrich Hertz in the late 1880's [23]. Noise and pseudo-noise (not entirely random) waveforms are inherently UWB and have a high relevance to NDT, as high bandwidths correspond to finer resolutions. A major benefit of these UWB waveform is that since the energy of the waveform lies across a wide range of frequencies, when incident on a dielectric composite material, there is a higher likelihood of some of the energy penetrating the sample [24].

Many current methods of noise radar employ a method of heterodyne correlation to extract the target responses [17]. Unlike traditional radar methods that convert a signal to baseband (by removal of the carrier signal), these noise radars process the signal, through analog or digital processes, directly at an intermediate frequency (IF) with ease. This ability is based on the advancements in analog-to-digital converter (ADC) technologies that make faster sampling rates and larger storage capabilities possible.

The advantage of UWB noise radars is that they have a low-probability of intercept (LPI), high immunity to jamming, and the capability of effectively reducing target masking, that is, revealing electrically small targets in the presence of electrically large ones—but when not accounted for, the randomness of these waveforms may cause residual fluctuations in the range profiles, leading to high peak-to-sidelobe ratios (PSLR). These high PSLRs tend to mask electrically small targets in the presence of electrically large targets, but through application of amplitude weighting functions or optimally selected pseudo-random noise waveforms, the discontinuities at the pulse boundaries (in the time-domain) may be reduced, resulting in higher PSLRs and more reliable defect detection and localization results.

The goal of this thesis, and research as a whole, is to develop a NDT microwave imaging method that utilizes noise waveforms to classify boundaries and discontinuities in multilayer

materials, such as those seen in CRFP and GFRP based samples subject to impact damages, galvanic corrosion, and any other means by which a material may develop internal flaws. This thesis is organized as follows: Chapter 2 discusses an overview of the electromagnetics at play when dealing with multilayered structures, how EM waves are reflected and transmitted at boundary locations, and the processing taking place to observe the collected data; Chapter 3 describes common UWB waveforms used in literature as well as outlines the development of pseudo-random noise pulses based on a white-noise random process; Chapter 4 serves as a description, on the component and system level, of the microwave imaging system operating in the X-band frequency range that has been designed at Penn State's Radar and Communications Laboratory for investigation of multilayered materials; Chapter 5 presents results of tests conducted on samples that represent real-world conditions that composite materials may undergo; and Chapter 6 serves as a conclusion and discussion of possible future work.

Chapter 2 Fundamentals

2.1 Electromagnetic characteristics of Multilayered Materials

The manner in which an electromagnetic (EM) signal interacts when it comes in contact with a certain structure is heavily dependent on the constitutive parameters of the material itself. When a nonmagnetic material is subject to an incident electric field, the dipoles within the molecular structure become polarized in the direction of the applied electric field, E . As the E -field increases, the dipoles polarization becomes stronger and causes an increase in the amount of potential energy stored within the material. The *relative permittivity* or *dielectric constant* is the measure of the amount of EM field lines within the material and represents the materials ability to store energy, which is given by

$$\epsilon_r = 1 + \frac{P}{\epsilon_0 E} \quad (2.1)$$

where P is the polarization strength of the dipoles and ϵ_0 is the permittivity of free space. The relative permittivity may be obtained by following the model of a harmonic oscillator [25], leading to the following complex expression

$$\epsilon_r = 1 + \frac{\frac{Nq^2}{\epsilon_0 m}}{(\omega_0 - \omega^2) + j\omega \left(\frac{k}{m}\right)} \quad (2.2)$$

where,

q is the dipole charge (units:[C])

N is the number of dipoles per unit volume (dimensionless quantity)

m is the mass of an electron or *standard mass* (units:[kg])

ω_0 is the resonance (angular) frequency of the oscillator (units:[rad/s])

ω is the angular "frequency" of the applied AC field driving the oscillator (units:[rad/s])

k is the damping coefficient of the oscillator (dimensionless quantity)

Equation (2.2) may be then represented by its real and imaginary components in the form

$$\varepsilon_r = \varepsilon_r' - j\varepsilon_r'' \quad (2.3)$$

where ε_r' is the absolute relative permittivity (related to the displacement current) regarding the materials ability to store energy and ε_r'' , is the absolute loss factor (related to static and alternating conductivities), regarding the materials ability to absorb energy [1].

The relationship between the real and imaginary parts of the complex permittivity are known as the Kramers-Kronig relation [26], given as

$$\varepsilon_r'(\omega) = 1 + \frac{2}{\pi} \int_0^{\infty} \frac{\omega' \varepsilon_r''(\omega')}{(\omega')^2 - \omega^2} d\omega' \quad (2.4a)$$

$$\varepsilon_r''(\omega) = \frac{2\omega}{\pi} \int_0^{\infty} \frac{1 - \varepsilon_r'(\omega')}{(\omega')^2 - \omega^2} d\omega' \quad (2.4b)$$

which are dependent upon the frequency, ω , of the time-varying electric field. These expressions are sometimes conveniently analogous to the relation between resistance and reactance in classical circuit theory.

When no fields are present, a material will have a static DC conductivity, σ_s , but when the material is in the presence of an AC field, an effective conductivity of the material is given as

$$\sigma_e = \sigma_s + \sigma_a = \sigma_s + \omega \varepsilon_0 \varepsilon_r'' \quad (2.5)$$

where σ_a is due to the dipoles oscillating in the presence of an alternating field. This conductivity due to the applied AC field in turn causes heating of the dielectric material and the absorption of EM energy [25]. This is the same reasoning behind how microwave ovens work.

If we now assume a uniform plane wave (a field that is not a function of the coordinates that form the equiphase and equiamplitude planes) propagating in the z direction, with the electric field polarized in the x direction, and amplitude E_0 , which is normally incident on a the interface between two semi-infinite media, the expressions for the electric field can be written as

$$\mathbf{E}^i = \hat{\mathbf{a}}_x E_0 e^{-\alpha_1 z} e^{-j\beta_1 z} \quad (2.6a)$$

$$\mathbf{E}^r = \hat{\mathbf{a}}_x \Gamma^b E_0 e^{+\alpha_1 z} e^{+j\beta_1 z} \quad (2.6b)$$

$$\mathbf{E}^t = \hat{\mathbf{a}}_x T^b E_0 e^{-\alpha_1 z} e^{-j\beta_1 z} \quad (2.6c)$$

where $\alpha \left[\frac{Np}{m} \right]$ is the attenuation constant, $\beta \left[\frac{rad}{m} \right]$ is the phase constant is the medium in which the wave is traveling [4], and Γ^b and T^b are the reflection and transmission coefficients, respectively, at the interface of the boundary. The associated magnetic fields may be found using the right-hand procedure or following Maxwell's equations as

$$\mathbf{H}^i = \hat{\mathbf{a}}_y \left(\frac{E_0}{\eta} \right) e^{-\alpha_1 z} e^{-j\beta_1 z} \quad (2.7a)$$

$$\mathbf{H}^r = -\hat{\mathbf{a}}_y \left(\frac{\Gamma^b E_0}{\eta_1} \right) e^{+\alpha_1 z} e^{+j\beta_1 z} \quad (2.7b)$$

$$\mathbf{H}^t = \hat{\mathbf{a}}_y \left(\frac{T^b E_0}{\eta_2} \right) e^{-\alpha_1 z} e^{-j\beta_1 z} \quad (2.7c)$$

For the discussion of reflections and transmission of multiple interfaces, we will neglect the effect of the attenuation constant and simply generalize the characteristics of a traveling EM waves traveling within a multilayer material.

First, we define the *reflection coefficient* parameter at media boundary as the ratio of the reflected electric field to that of the incident electric field as

$$\Gamma^b = \frac{\eta_2 - \eta_1}{\eta_2 + \eta_1} = \frac{E^r}{E^i} = -\frac{H^r}{H^i} \quad (2.8)$$

where η represents the intrinsic impedance of a material given by

$$\eta = \sqrt{\frac{\mu}{\varepsilon}} \quad (2.9)$$

where

$$\varepsilon = \varepsilon_0 \varepsilon_r \quad (2.10)$$

and

$$\mu = \mu_0 \mu_r \quad (2.11)$$

Here μ_0 is the permeability of free space and μ_r is the relative permeability of the material. The portion of the wave transmitted into media 2 is governed by the *transmission coefficient*, given by

$$\Gamma^b = \frac{2\eta_2}{\eta_1 + \eta_2} = 1 + \Gamma^b = \frac{E^t}{E^i} = \frac{\eta_2 H^t}{\eta_1 H^i} \quad (2.12)$$

For the expanded case of a material with N -layers, as shown in Figure 2-1, the overall input reflection coefficient of the N -layer material may then be approximated by the expression

$$\Gamma_{in} \cong \Gamma_0 + \Gamma_1 e^{-j2\beta_1 d_1} + \Gamma_2 e^{-j2(\beta_1 d_1 + \beta_2 d_2)} + \dots + \Gamma_N e^{-j2(\beta_1 d_1 + \beta_2 d_2 + \dots + \beta_N d_N)} \quad (2.13)$$

where

$$\Gamma_0 = \frac{\eta_1 - \eta_0}{\eta_1 + \eta_0} \quad (2.14a)$$

$$\Gamma_1 = \frac{\eta_2 - \eta_1}{\eta_2 + \eta_1} \quad (2.14b)$$

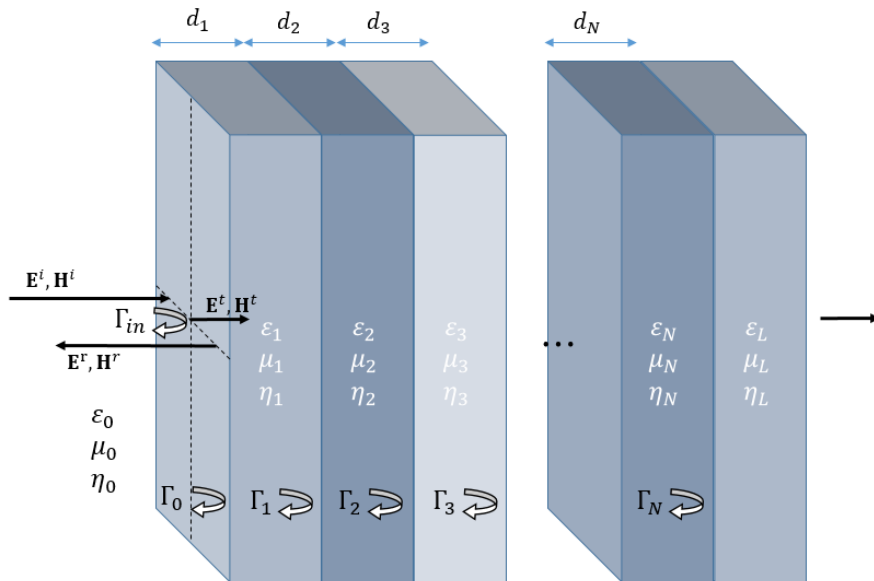


Figure 2-1: Normal EM wave propagation through an N -layered multilayer material (adapted from [26]).

$$\Gamma_2 = \frac{\eta_1 - \eta_0}{\eta_3 + \eta_2} \quad (2.14c)$$

$$\vdots$$

$$\Gamma_N = \frac{\eta_L - \eta_N}{\eta_L + \eta_N} \quad (2.14d)$$

Equation 2.13 is simulated for the case of a CFRP composite coupled to a perfect electric conducting (PEC) backing plate for the cases of *no damage* and with *damage*, in an attempt to model internal delaminations. For the simulations, the total thickness of the CFRP is 6.4 mm and the delaminations are modeled as air gaps of thickness 0.1mm and 0.05mm, each placed at 0.025 mm and 3.25 mm, respectively, as shown in Figure 2-2a. The relative permittivity was chosen as $\epsilon_r = 50$ [27], assuming the electric field is orthogonal to the fiber direction. The application of equation 2.13 is shown in Figure 2-2b, where we can see only minimal differences are visible.

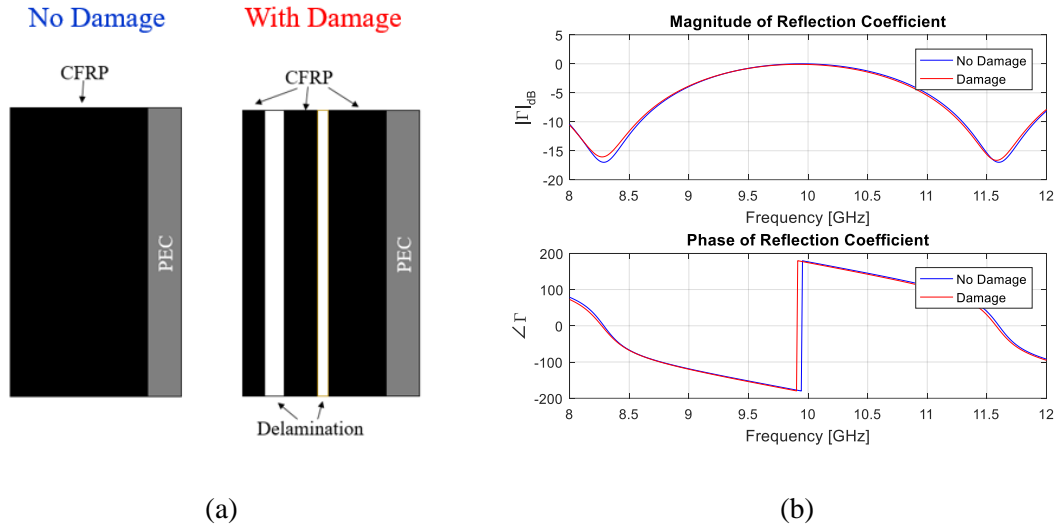


Figure 2-2: (a) Model of CFRP without and with internal delaminations and (b) calculated reflection coefficient (application of equation 2.13) for each case.

2.2 Operational Fundamental of Radar Systems

Simply put, the objective of a traditional pulsed radar is to emit an EM pulse from a transmitting antenna (Tx) and wait for any reflections from a target to appear at the input of the receiving antenna (Rx). Based on the received signal, the distance, velocity, and/or relative size of the object may be determined.

All pulsed radar systems operate under one of the following antenna configurations: monostatic, where a single antenna is used as the Tx and Rx antennas; bistatic, where separate antennas are used for Tx and Rx antennas; multistatic, where there may be multiple Tx and Rx antennas; and pseudo-monostatic, where two separate Tx and Rx antennas are collocated, but operation is similar to bistatic. These configurations are summarized in Figure 2-3. A benefit of the pseudo-monostatic case is that the sensitive receiver is isolated from the high power transmitter.

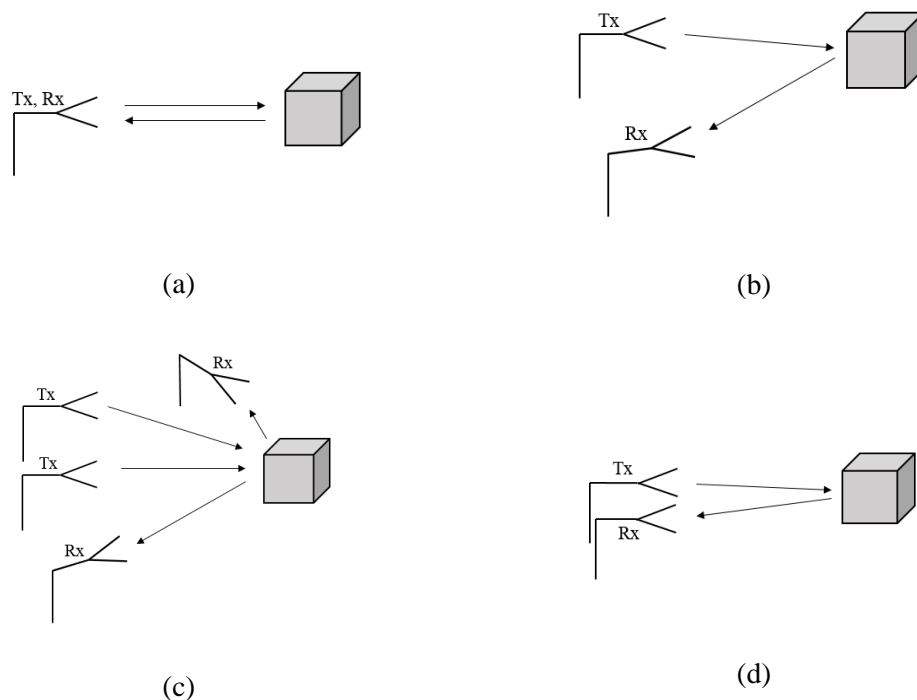


Figure 2-3: Available antenna configurations: (a) Monostatic, (b) bistatic, (c) multistatic, and (d) pseudo-monostatic.

The main features of pulsed radars are the carrier frequency, pulse length τ , pulse repetition interval (PRI) T_p , and the modulation within the pulses. For a reflection signal that arrives at time T , the range at which the reflection originated is determined by (assuming free-space)

$$R = \frac{cT}{2} \quad (2.15)$$

where c is the speed of light. Here is clear that if the round-trip time is measured, then based on the speed of the EM waves (the speed of light), it is possible to determine the distance from the radiating source to the unknown target.

2.2.1 Theoretical Range Resolution

The ability to view two separate targets at some distance from the aperture plane, as two separate targets, is limited to the theoretical range resolution, which is expressed by

$$\Delta R = \frac{c}{2B} \quad (2.16)$$

where B is the bandwidth of the transmitted signal. What may be drawn from this relation is that if two targets are separated at a value larger than the range resolution, they will be able to be recognizable as two individually spaced targets. When the separation between the two targets becomes smaller than the calculated range resolution from equation 2.16, then they will appear as one. Therefore, the tradeoff that must be made for finer resolutions is using a signal of higher bandwidth, which in turn requires RF components capable of handling higher bandwidths and analog-to-digital converters (ADC) that are capable of handling higher bandwidths—either way, higher bandwidth systems results in higher system development costs.

2.2.2 Signal-to-Noise Ratio of Systems

A primary requirement of the radar receiver is to maintain a high signal-to-noise ratio (SNR), which allows for a higher sensitivity to weakly reflective targets or signals that have undergone more attenuations. Many factors will result in poor SNRs, such as electrically small targets, noisy environments, and high system noise—summarized as either external or internal noise. The SNR of a radar system is defined as the ratio of the received power to that of the noise power, given by [28]

$$SNR = \frac{P_r}{P_n} = \frac{P_t G_t G_r \sigma \lambda^2 G_p L}{(4\pi)^3 R^4 k_B T_s B_n} e^{-4\alpha R} \quad (2.17)$$

where,

P_r is the received power (units: [W])

P_t is the transmitted power (units: [W])

G_t is the transmitting antenna gain (dimensionless quantity)

G_r is the receiving antenna gain (dimensionless quantity)

σ is the radar cross section (RCS) of the target (units: [m^2])

λ is the wavelength of signal (units: [m])

G_p are the processing gains (dimensionless quantity)

L are the losses due to cables, connectors, etc. (dimensionless quantity)

R is the range to target (units: [m])

$e^{-4\alpha R}$ are the losses within the propagation medium, over twice the targets range (dimensionless quantity)

For a receiver at a standard temperature of T_0 (given in Kelvin) and a system noise bandwidth of B , the the associated noise power P_n is given by

$$P_n = k_B T_0 B_n \quad (2.18)$$

where $k_B = 1.38 \times 10^{-23} \left[\frac{\text{J}}{\text{K}} \right]$ is the Boltzmann constant. Other components such as cables, antennas, mixers, and amplifiers will also add system noise, which leads to the definition of a system noise temperature, T_s . Now the noise power is related to the system noise temperature by

$$P_n = k_B T_s B_n \quad (2.19)$$

The effectiveness of the receiver depends on four factors: the noise figure (NF); the Boltzmann constant multiplied by temperature ($k_B T_s$); the noise bandwidth of the system; and the SNR. Since the $k_B T_s$ term is constant for the most part, the bandwidth is chosen by design specifications, and since the SNR cannot be improved once the signal reaches the receiver, the NF must be optimized to achieve good performance. A low NF will provide a higher SNR in an analog receiver and will also allow for lower transmitting powers to achieve the same system performance [29].

The ratio of the SNR of the input signal to the SNR of the output signal is known as the *noise factor*, which is a dimensionless quantity given by

$$F = \frac{\text{SNR}_{\text{in}}}{\text{SNR}_{\text{out}}} = \frac{P_{r,\text{in}}/P_{n,\text{in}}}{P_{r,\text{out}}/P_{n,\text{out}}} \quad (2.20)$$

The noise factor may then be given by its 10 times log version which is known as the *noise figure*

$$NF = 10 \log_{10}(F) = 10 \log_{10} \left(\frac{\text{SNR}_{\text{in}}}{\text{SNR}_{\text{out}}} \right) \quad (2.21)$$

A typical receiver is designed using active and passive components, where the noise figure of each component must be accounted for. In the case of passive components, such as filters and attenuators, the noise factor is given by

$$F = 1 + (A - 1) \frac{T_s}{T_0} \quad (2.22)$$

where, A is the amount of attenuation of the device. The noise factor of a cascaded system may then be represented using Friis' formula as

$$F_{\text{cas}} = F_1 + \frac{F_2 - 1}{G_1} + \frac{F_3 - 1}{G_1 G_2} + \dots + \frac{F_N}{G_1 G_2 \dots G_{N-1}} \quad (2.23)$$

Where F_n is the noise factor and G_n is the gain of the n -th component. From this equation, the noise factor of the system may be controlled somewhat by placing a component—typically a low-noise amplifier (LNA) (discussed in further detail in Chapter 4)—with a low noise factor as the first component in the receiver chain (directly after the Rx antenna). The advantage of equation 2.23 is shown for the case of a hypothetical radar receiver with and without a LNA with a low noise factor in Figure 2-4. This image displays that using an LNA allows the SNR of the receiver to remain high, while minimizes the NF of the receiver.

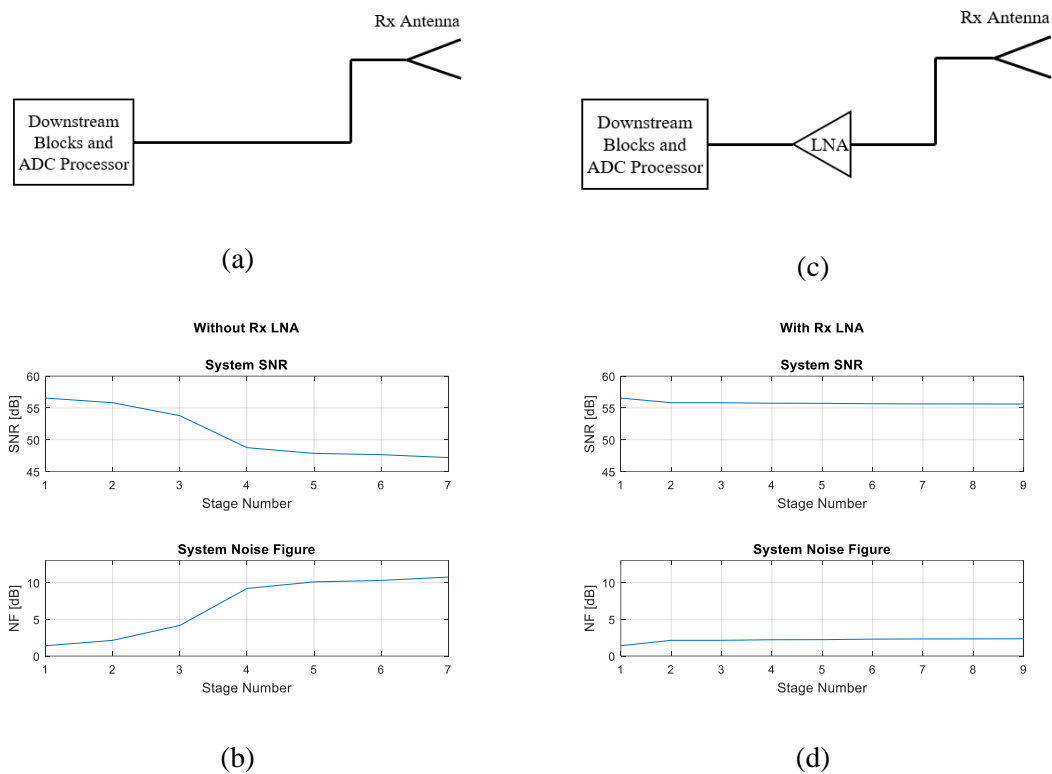


Figure 2-4: Comparisons of SNRs and NFs of radar receivers without (a & b) and with (c & d) a LNA with low noise factor after the receiving antenna.

2.2.3 Matched Filtering via Digital Cross-Correlation

The use of a correlation receiver is wide-spread and commonly used method in various radar applications to increase the signal-to-noise ratio (SNR). Target detection in noise radars is implemented through the matched filtering approach, which is executed using cross-correlation [30]. In the case of the classical continuous wave noise radar, the correlation process takes place by mixing the reflected signal with a time-delayed replica of the original transmit signal. If the replica is delayed by the same amount of time as the main echo in the received signal, a peak value will occur at the center of the output.

This operation may be executed digitally, similar to [31] by saving the received and a reference signal (copy of the transmitted signal) to separate channels of an analog-to-digital converter. For a pseudo-random noise waveform, the cross-correlation of the digitally sampled datum takes the form

$$r_{xy}[z] = \sum_{n=-\infty}^{\infty} x[z]y[n-z], \quad z = 0, \pm 1, \pm 2, \dots \quad (2.25)$$

where $x[z]$ is the reference signal and $y[n]$ is the received radar signal—this expression is valid provided the infinite sum converges [32]. The variable z here represents the *lag* parameter, which corresponds to a time-shift between the two signals. The cross-correlation process may also be calculated in the frequency domain as

$$r_{xx}[z] = x[z] \otimes y[z] = \mathcal{F}^{-1}\{\mathcal{F}\{x[z]\} \cdot \mathcal{F}^*\{y[z]\}\} \quad (2.26)$$

where \otimes is the correlation operation (in compact form) and $\mathcal{F}\{\cdot\}$ and $\mathcal{F}^{-1}\{\cdot\}$ are the Fourier and inverse Fourier transforms. If signal is cross-correlated with itself, this operation is then known as autocorrelation given by

$$r_{xx}[z] = \sum_{n=-\infty}^{\infty} x[z]x[n-z], \quad z = 0, \pm 1, \pm 2, \dots \quad (2.27)$$

which as we will see in Chapter 3 will serve as our basis for identifying noise waveforms that will yield imaging results similar to other waveforms used in imaging applications. The output of 2.27 for a pseudo-random noise pulse is shown in Figure 2-5. What we will see is that due to the randomness of these waveforms, the sidelobes will vary between high and low values based on rapid changes (discontinuities) in the original time-series representation of the signal.

If we look at the normalized spectral and cross-spectral densities, that is, the Fourier transforms of the raw unprocessed received data and the output of the matched filter, in Figure 2-6, it is clear that by using the cross-correlation operation we are able to significantly increase the SNR of the received radar data.

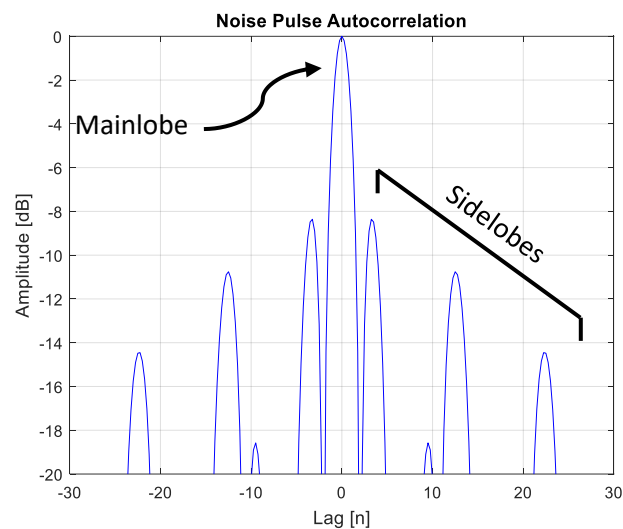


Figure 2-5: Autocorrelation output of noise sequence.

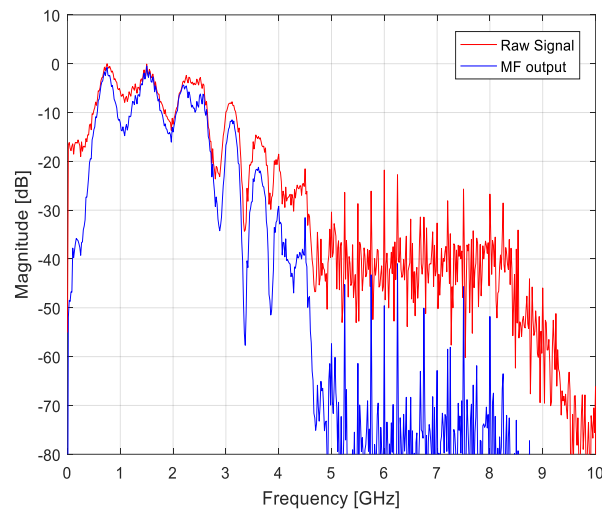


Figure 2-6: Comparisons of the spectral content of the raw radar data (red trace) and the cross-spectral data of output of the cross-correlation operation (blue trace). Applying the matched filter significantly increases the overall SNR of the radar receiver.

2.2.4 Coherent Pulse Integration

Higher SNRs are also achievable through coherent integration (or coherent averaging) of multiple pulses over a set span of time. This operation is possible by many oscilloscopes at the expense of longer acquisition periods, but may be done afterwards through signal processing.

To start the data collection for this type of averaging, acquisition must be preceded with a trigger pulse to start the collection process. Data are collected for a range of samples that encompasses the returns from a single pulse. Afterwards another trigger pulse is sent, to denote the start of acquisition for the echo data from a second pulse, and again, after the same amount samples have been taken, the waveform is saved. This processes is repeated for N pulses (or N averages).

Consider the case when you have a burst of N equally-spaced (in time) pulses that are reflected off of a point target (assuming a stationary antenna platform) down-range. Coherent

averaging decomposes the burst returns down into individual PRIs, sums each at an index value, and divides by the total by the number of pulses, following

$$\bar{s}_{avg}[n] = \frac{1}{N_p} \sum_{i=1}^{N_p} s_i[n] \quad (2.27)$$

Where s_i is the data for each pulse, N_p is the number of pulses in the entire burst, and n is the current index value. The bar over the output represent the averaged output, but in the remainder of this thesis is will be disregarded as it will be assumed there has been averaging applied.

To demonstrate this, a 2-ns white-noise pulse with an SNR of 10 dB was created and shown in Figure 2-7 (left side). Applying 2.27 with $N = 50$, the resulting output waveform is better defined and shows less noise artifacts. What can be gathered is that for a given SNR, the noise of the signal may be reduced as the number of averages is increased. Also, it can be seen is that for an SNR of 10 dB, the echo signal is nearly indiscernible, but with averaging, the low energy noise pulse is now detectable.

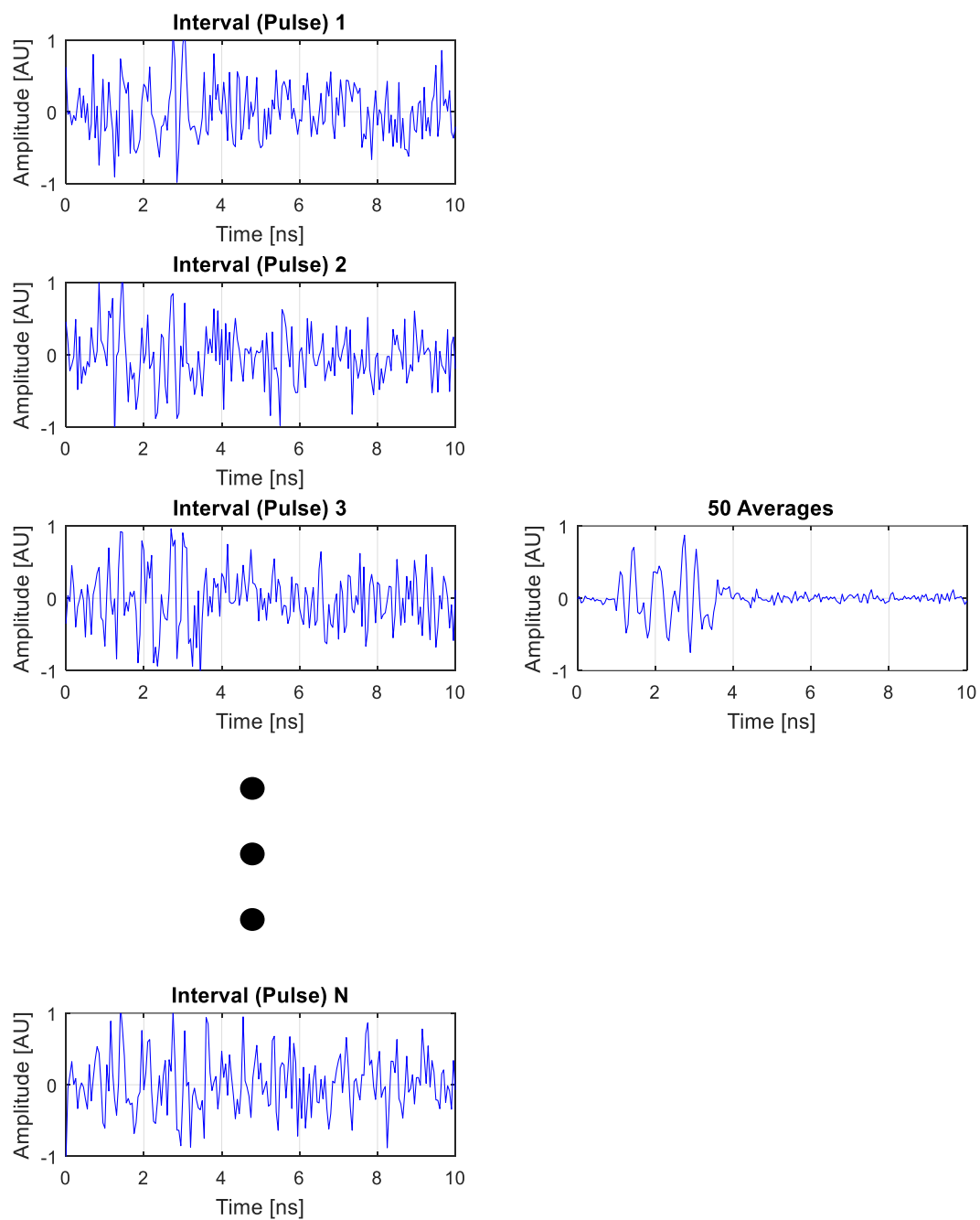


Figure 2-7: Benefits of coherent pulse integration. SNR of 2-ns white-noise signal corrupted with external noise (left) increased after integration of 50 pulses (right).

Now, if we observe the effect of noise on the output of the matched filtering operation—and ignore other losses (components losses, propagation losses, and attenuation losses)—the output of the matched filter may also be corrupted by noise to the extent that target detection is no longer possible, where small reflections may be lost in the noise.

To demonstrate this, two targets were simulated at separate ranges from the antenna's aperture plane (actual ranges not relevant for demonstration purposes), yielding delayed reflections present in the received signal, as depicted in Figure 2-8. Now, based on this configuration, the corresponding output of the matched filter operation is shown for SNRs at the receiver of 0 dB, 10 dB, and 20 dB—each SNR measurement is shown for the cases of no averaging and for 5, 30, and 60 averages—in Figures 2-9 through 2-11.

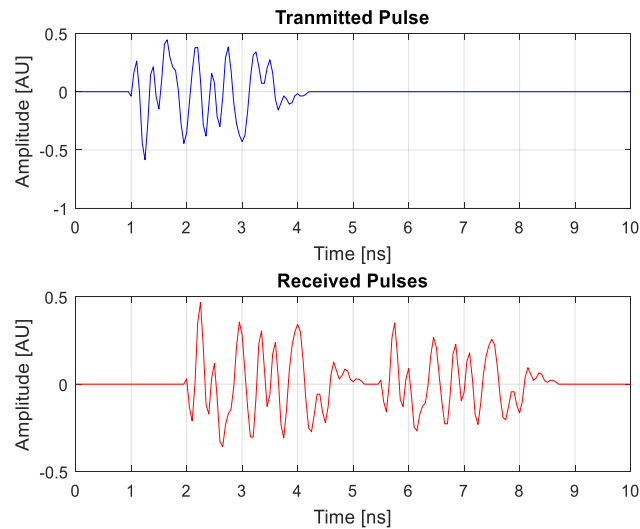


Figure 2-8: Simulated transmitted pulse and reflected pulses from two closely separate scatterers.

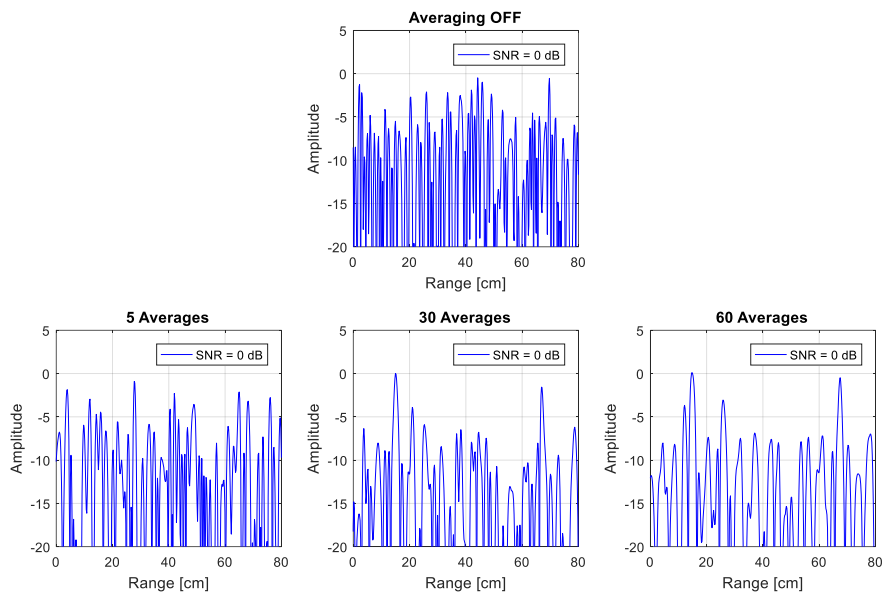


Figure 2-9: Matched filter output for 0 dB SNR on receive, shown for 5, 30, and 60 coherent pulse integrations.

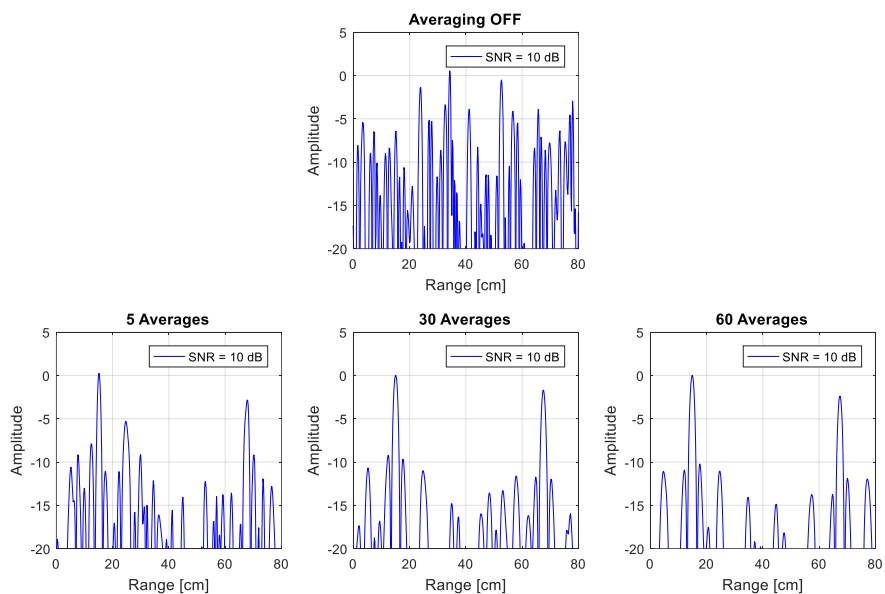


Figure 2-10: Matched filter output for 10 dB SNR on receive, shown for 5, 30, and 60 coherent pulse integrations.

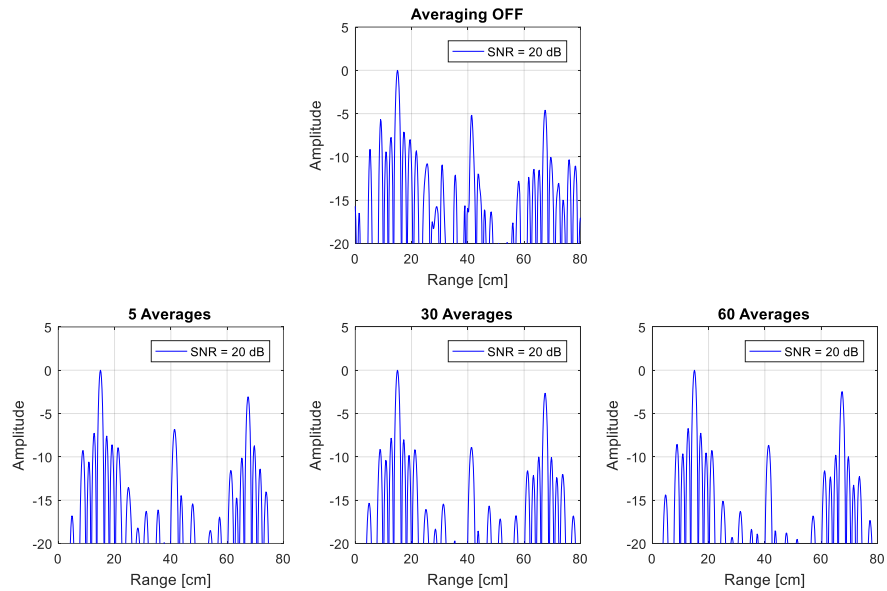


Figure 2-11: Matched filter output for 20 dB SNR on receive, shown for 5, 30, and 60 coherent pulse integrations.

The trade-off that must then be kept in mind is that there must be a tipping point, as discussed in [33, 34] where the system SNR may be kept high enough so that the amount of necessary averages is reduced. Hence, as the SNR increases, the amount of averages needed decreases, and therefore the number of necessary samples to be acquired also reduces, which leads to decreases in processing time. Additionally, since the choice of stand-off distance (SOD) from the material is kept as a design parameter, the output power of the system may also be changed to account for attenuation through various material, again reducing processing costs (time and data lengths) due to increases in SNR.

Chapter 3 Waveforms for NDT Microwave Imaging

In this chapter, we discuss various types of waveforms used in typical radar applications, such as, target ranging, ground-penetrating radar, synthetic aperture radar (SAR), NDT, and medical tomography. Following, metrics for predicting how well each waveform will operate in actual test environments are investigated through simulated results.

The most simple pulses consist of two controllable parameters, the amplitude A and the pulse duration τ . These have a direct connection to possible range resolution, as well as how well a signal may be detected. The energy associated with a simple pulse is given by $A^2\tau$. This leads to an unfortunate tradeoff, where detection is related to pulse energy and resolution is related to pulse duration. Hence, a better range resolution is achieved by using shorter pulses and better detection is achieved by longer pulses carrying more energy.

3.1 Ultrawideband Waveforms

Pulse compressed waveforms are an alternate to the standard simple pulse. Through frequency or phase modulation, higher resolutions are achievable while maintaining adequate detection level.

3.1.1 Linear Frequency Modulated Chirp Waveforms

A common form of UWB pulse compressed waveform is the linearly frequency modulated (LFM) chirp pulse, given in its complex-form as

$$x(t) = A \exp[j\theta(t)] = A \exp\left[j\pi\left(\frac{Bt^2}{\tau}\right)\right] \quad (3.1)$$

where A is the amplitude envelope of transmitted signal, B is the signal bandwidth, τ_p is the pulse duration, and t is defined over the interval $0 < t < \tau_p$. Such a waveform with $B = 4$ GHz and pulse duration $\tau = 10$ ns is shown in Figure 3-1.

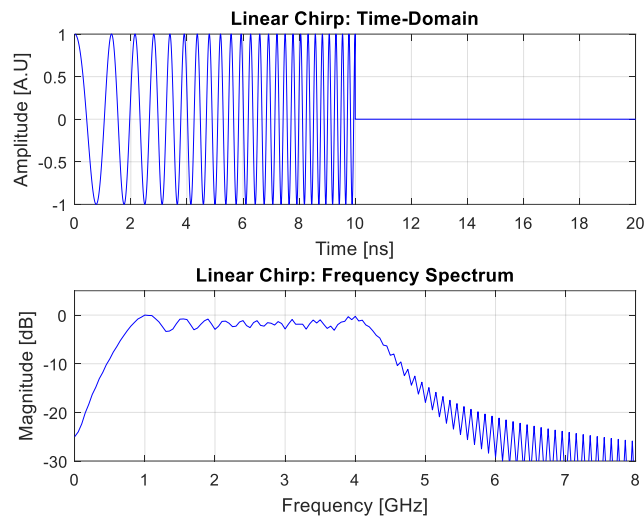


Figure 3-1: Time and frequency domain representation of LFM chirp pulse.

The instantaneous frequency of this type of waveform is the time derivative of the phase function as

$$F_i(t) = \frac{1}{2\pi} \frac{d\theta(t)}{dt} = \frac{B}{\tau_p} t \quad (3.2)$$

Where when B is positive the waveform is considered an *upchirp* and when B is negative is considered a *downchirp*.

3.1.2 Gaussian-Modulated Sinusoidal Pulses

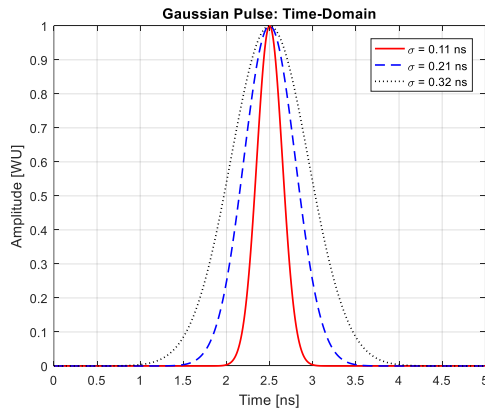
The next type of UWB signal is the short duration Gaussian pulse, represented by

$$s(t) = \exp\left[-\frac{(t - t_0)^2}{2\sigma^2}\right] \quad (3.3)$$

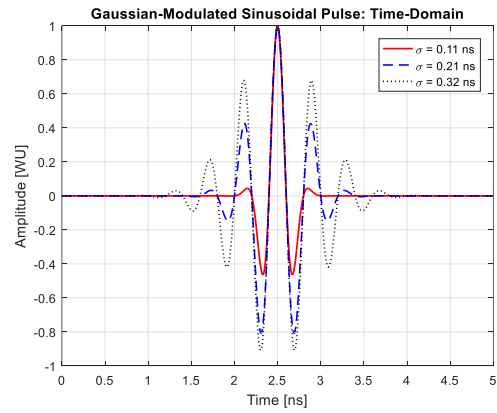
where σ is the standard deviation of the pulse (given in seconds), which is related to the pulse duration by $\tau_p = 2\pi\sigma$. The t_0 variable corresponds to a time delay. The time-domain representation of this type of Gaussian waveform is shown in Figure 3-2a and the frequency domain representation in 3-2b. A problem with this standard Gaussian pulse is the fact that its frequency domain representation includes a DC component, which is unable to propagate in free-space [35]. Alternatively, a Gaussian-modulated sinusoidal pulse (GMSP) may be used, which allows for a greater ability to shape the frequency domain of the signal. Such a signal may be represented as

$$s(t) = \cos(2\pi f_c t) \exp\left[-\frac{(t - t_0)^2}{2\sigma^2}\right] \quad (3.4)$$

with f_c representing the center frequency of the signal having a pulse width of τ_p . Figure 3-2c shows the time-domain representation and Figure 3-2d shows the frequency domain representation of a Gaussian-modulated sinusoidal pulse for varied values of σ .



(a)



(c)

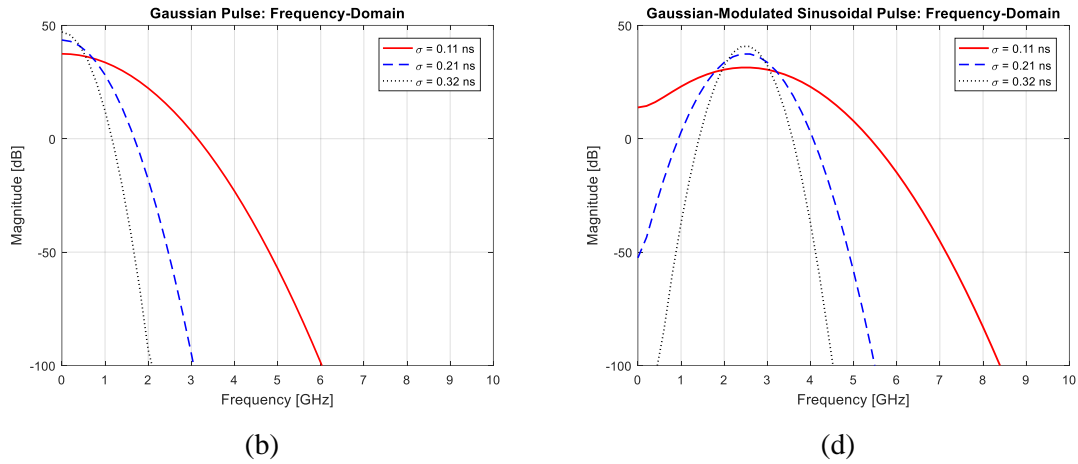


Figure 3-2: Comparisons of time and frequency domains of standard Gaussian pulses (a) and (b) and sinusoidal-modulated Gaussian pulses (c) and (d), for different values of σ .

3.1.3 Pseudorandom Noise Pulses

Classically, UWB random noise signals have been created through amplification of thermally-generated noise [24] and pseudorandom noise signals through digital design in a computer aided software.

We start off assuming a white noise random process, as in [36] that can be created through the summation of N sinusoids each with frequency, f , random phase, ϕ , and of duration T . Now, we shall choose the range of the N sinusoids frequencies to be on the interval

$$f_{min} \leq f \leq f_{max} \quad (3.5)$$

which make up the frequency vector

$$f = [f_1, \dots, f_n] \quad (3.6)$$

A similar approach is done for the phase, but now, the phase components on the interval

$$0 \leq \phi \leq 2\pi \quad (3.7)$$

are chosen at random to create the phase vector

$$\phi = [\phi_1, \dots, \phi_n] \quad (3.8)$$

The resulting white noise random signal may then be described by the following expression,

$$x[(f_1, \phi_1), \dots, (f_n, \phi_n), t] = \sum_{k=1}^N \frac{\sqrt{2}A_0}{\sqrt{N}} \sin(2\pi f_k t + \phi_k) u(t) \quad (3.9)$$

where A_0 represents the amplitude of the sinusoids, N is the number of individual sinusoids contained within the set, and $u(t)$ represents the unit step function. The resulting signal, based on equation (3), represents a random white noise process covering all frequencies across the frequency spectrum (assuming f_{max} is large). The application of equation (3.9) is shown in the time and frequency domain in Figures 3-3a and 3-3b, respectively, for $N = 1000$ and $A_0 = 1$.

Since RF hardware is limited to a finite frequency range of operation and frequency band occupation is critical, the signal should be bandlimited to a specified range on the interval $[f_0, f_1]$. Following sinusoidal steady-state theory, the bandlimited version of equation (3.9) takes the form

$$s[(f_1, \phi_1), \dots, (f_n, \phi_n), t] = \sum_{k=1}^N A(f_k) \frac{\sqrt{2}A_0}{\sqrt{N}} \sin(2\pi f_k t + \phi_k + \phi(f_k)) u(t) \quad (3.10)$$

where $A(f_k)$ represents the amplitude variations due to the filter and $\phi(f_k)$ represents the phase shift, or group delay of the filter, each given by

$$A(f_k) = |H(j2\pi f_k)| \quad (3.11)$$

$$\phi(f_k) = \angle H(j2\pi f_k) \quad (3.12)$$

The application of equation (3.10), using a finite impulse response (FIR) bandpass filter with low and high cutoff frequencies of 0.5 GHz and 4.5 GHz, respectively, is shown in Figure 3-3c and 3-4d (see Appendix C for more information on FIR filters).

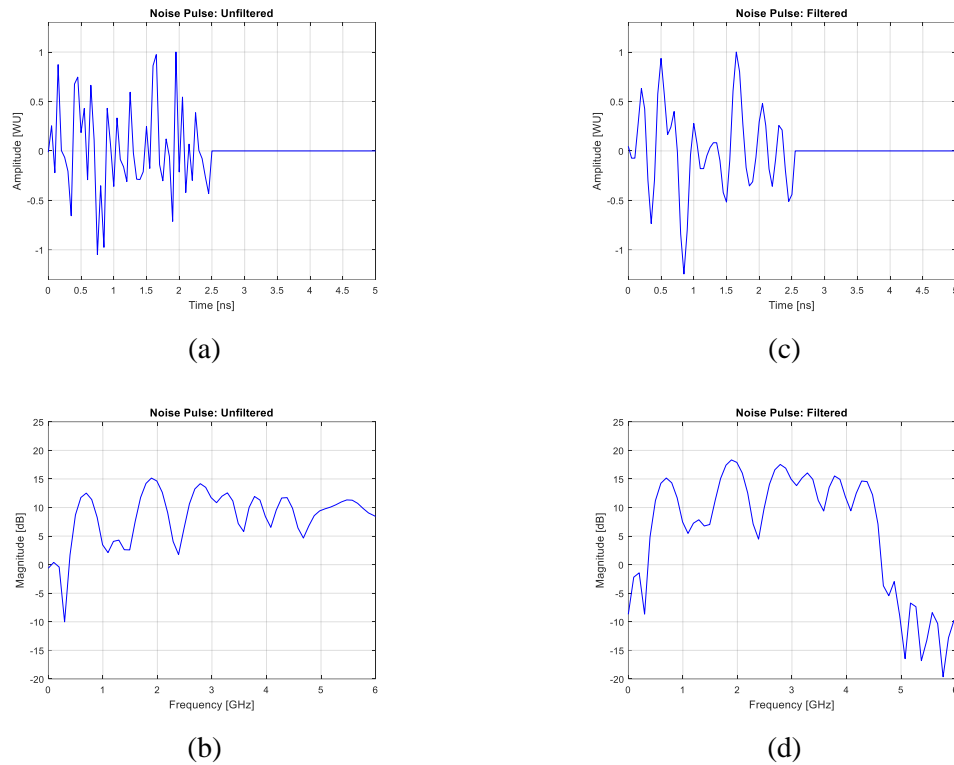


Figure 3-3: Time and frequency domain representations of application of equation (3) (a&b) and of equation (4) (c&d) for 1000 ($N = 1000$) separate sinusoids of random frequency and phase.

Noise signals may be designed in an alternative fashion to mimic the results of equation (4), while reducing the necessary processing. This is done by using a vector of random numbers with a Gaussian distribution over the range of -1 to $+1$ (using a random number generator) as discrete amplitude values to create the noise waveform. The resulting waveform is filtered through a FIR bandpass filter to limit the bandwidth of the signal, followed by multiplication with the unit step function to create the noise pulse. The time and frequency domain representations of this noise pulse are shown in Figure 3-4a and 3-4b.

To verify the equivalence of these two methods, it should follow from the central limit theorem that the amplitude at any chosen time, over N trials of waveform generations, should return an approximately Gaussian distribution. The probability density functions for both methods, over 250 trials, measured at 1.5 ns, are shown in Figure 3-5.

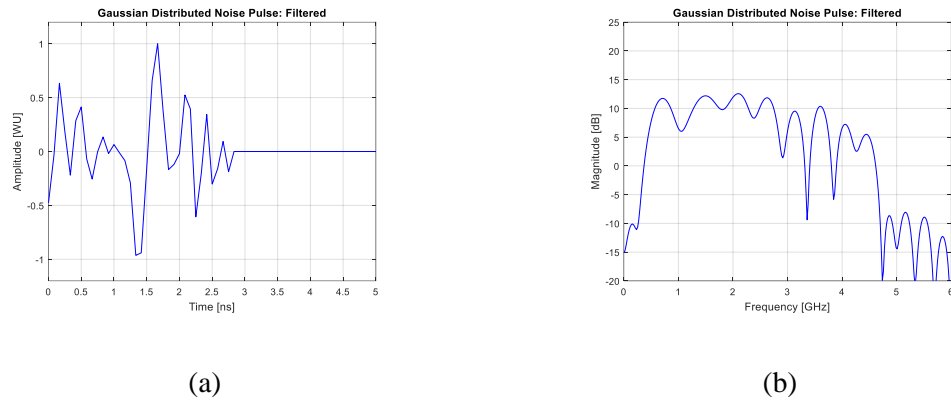


Figure 3-4: Alternate noise pulse generation method in the time-domain (a) along with the corresponding frequency spectrum (b).

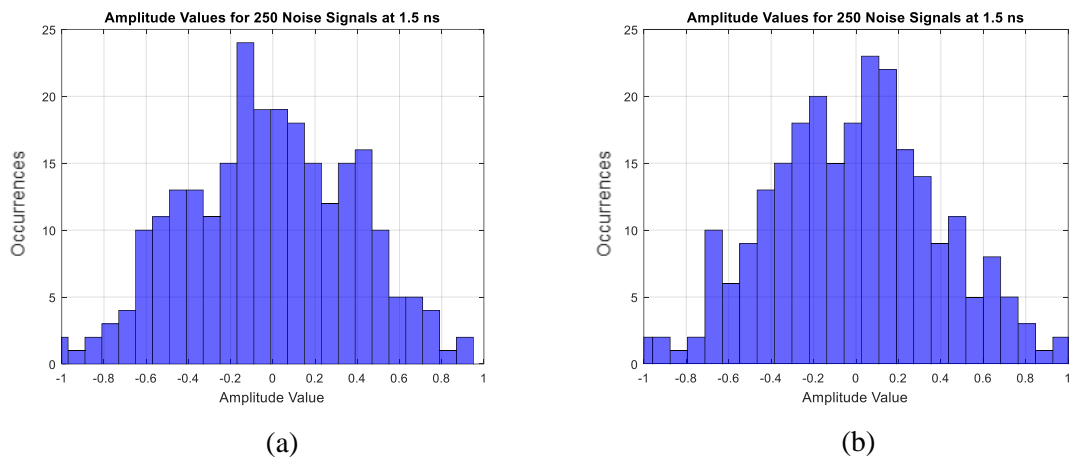


Figure 3-5: Histogram using of amplitudes of 250 noise signals measured at 1.5 ns while generating noise pulses using equation 8 (a) and while using a random number generator to assign amplitude values (b).

3.2 Waveform Performances

In this section metrics such as time-bandwidth products and peak-to-sidelobe ratios are discussed for noise based waveforms and compared to those of other waveforms discussed in section 3.1. These parameters have been discussed with focus on noise waveforms in [37, 38].

For a waveform to be considered pulse compressed it is assumed that its *time-bandwidth* product is greater than 1 ($B\tau > 1$). Waveforms with larger time-bandwidth products will be able to convey more energy to a target than that of ones with smaller time-bandwidth products. It is to be noted that the resolution in a pulse compression radar is independent of range and is related to the bandwidth of the signal [39]. Hence, pulse length is chosen based on desired pulse energy, while bandwidth is chosen based on desired range resolution.

An example of a white-Gaussian noise signal and the associated frequency spectrums are shown for time-bandwidth products of 10, 25, and 100 in Figure 3-6. The bandwidth used for each signal is 4 GHz, which leads to pulse length of 2.5 ns, 6.25 ns, and 25 ns. As can be seen, at the

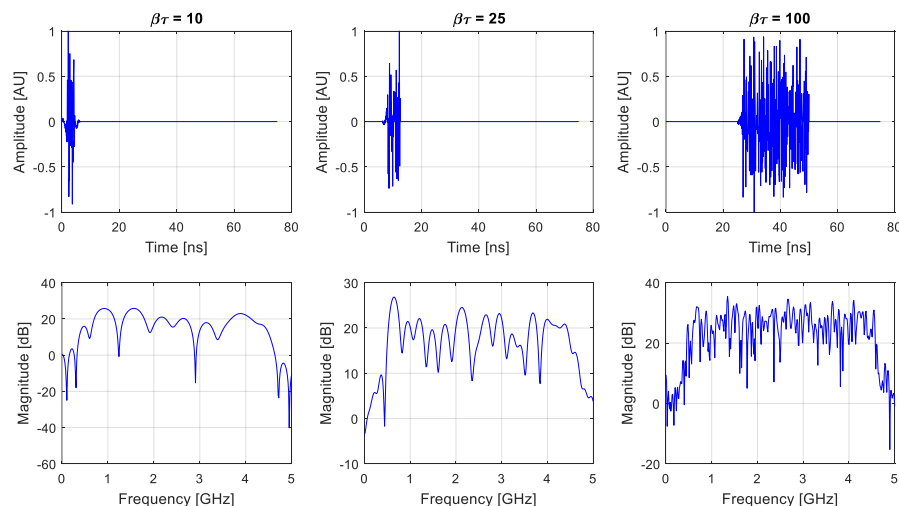


Figure 3-6: (Top row) Chirp signals for $\beta\tau = 10$, $\beta\tau = 25$ and $\beta\tau = 100$ and their frequency domain representations (bottom row).

time-bandwidth increases, there is more energy in the frequency domain representation of the signal.

A metric used for characterizing a waveform's effectiveness in resolving targets is called the *peak-to-sidelobe ratio* (PSLR), which is a measure of the matched filter's maximum output amplitude value to that of the value of the next highest sidelobe. A low PSLR will result in the inability to resolve electrically small targets in the presence of electrically large ones, which is called *target masking*. Since noise signals are random, the possibility arises that the PSLR of a given noise pulse may sometimes actually yield a PSLR worse than that of a commonly used waveform, such as the Gaussian-modulated sinusoidal pulse or chirp pulse of equal bandwidth.

Figure 3-7 shows a comparison of the best-case possible detection scenarios (no noise introduced into the simulation) of targets separated by 6 cm, for the case of a random noise pulse with a high PSLR in Figure 3-7a and for one with a low PSLR in Figure 3-7b. At target separation of 6 cm, the randomly generated noise waveform with a low PSLR is unable to accurately resolve the two targets, while the waveform with a high PSLR easily identifies the two targets. It is then a

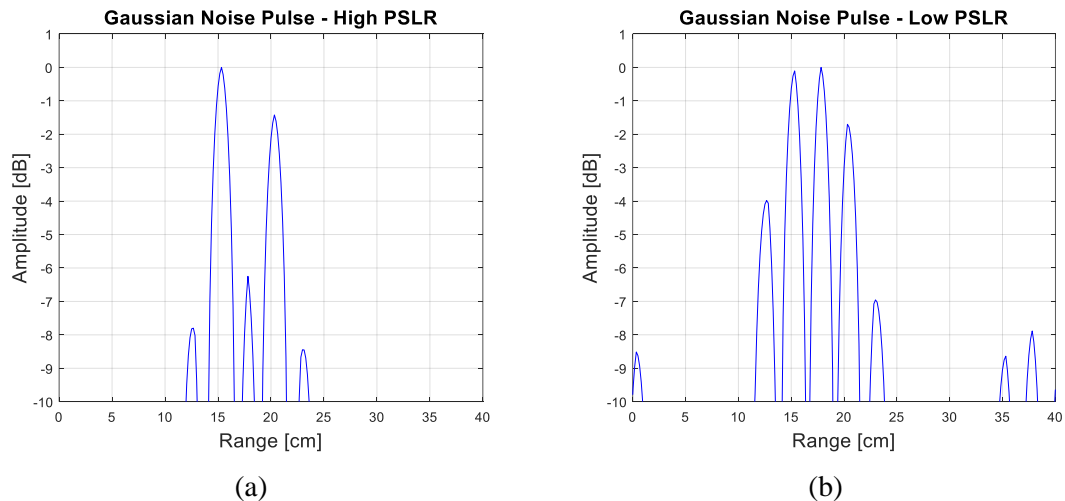


Figure 3-7: Simulated range profiles of scene with two targets separated by 6 cm while using a noise pulse with a high PSLR (a) and noise pulse with a low PSLR (b).

priority to choose (hence pseudo-random) a noise waveform with a large PSLR to utilize the full benefits of the noise waveform's capability of achieving extremely low sidelobes.

Figure 3-8 shows the measured PSLRs for 1000 separate iterations of noise pulses, showing a right-skewed quasi-Gaussian distribution. Here the PSLR values of a chirp signal and Gaussian-modulated sinusoidal pulse of equal bandwidth are shown for comparison. Typical criteria for a noise pulse to be chosen for microwave imaging is one that yields a PSLR value that is greater than that of comparison waveforms. Alternatively, the signal may be windowed in the frequency domain to reduce the, effectively time-domain, range profile sidelobes. The approach will typically foster acceptable PSLRs, but without as much control over numerical PSLR requirements. Separate amplitude weighting functions may be used in the range and azimuth dimension to reduce the sidelobe levels, but this is at the cost of increasing the width of the mainlobe.

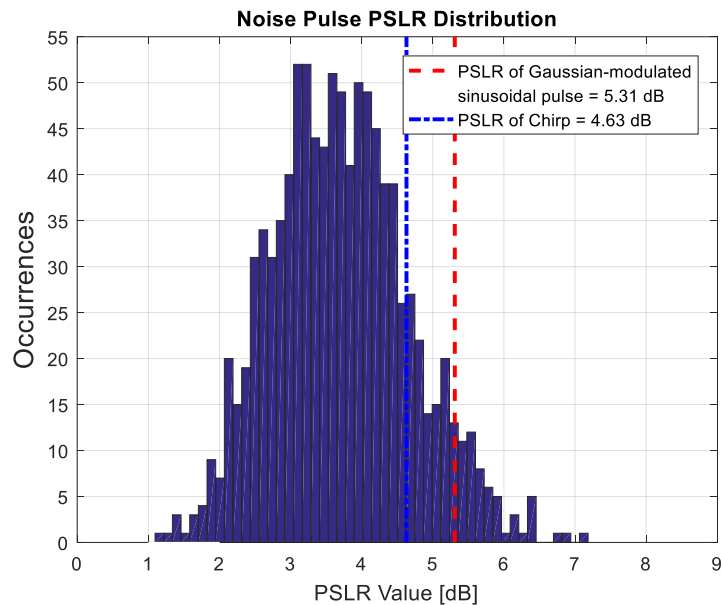


Figure 3-8: PSLR distribution for 1000 iterations of noise pulses with a bandwidth of 4 GHz. The dashed/dotted blue line represents the PSLR of a chirp and the dashed red line corresponds to the PSLR of a sinusoidal-modulated Gaussian pulse, both with bandwidth of 4 GHz

Chapter 4 NDT Microwave Imaging System Design and Performance

In previous chapters the governing relations for interactions of EM waves with multilayered boundaries and the development of UWB waveforms were discussed. Now, in this chapter the development of an UWB noise radar system used for NDT of multilayered materials will be explained. First, descriptions of the RF components and their operations will be discussed (in some cases simulations showing their characteristics will be given). Second, the overall imaging system will be discussed and be broken down into subsections consisting of the up-conversion channel, down-conversion channel, reference channel, and local oscillator (LO) conditioning channel.

4.1 RF Component Descriptions

Typical radar systems are made-up of various pieces of RF hardware, each with their own dedicated purpose. Many high-frequency radars use heterodyne topologies, which consist of stable local oscillators (LO), frequency conversion mixing devices, analog filters, power amplifiers (PA), low-noise amplifiers (LNAs), splitters (when necessary), antennas, and an assortment of passive attenuators. This section serves as a summary of devices functions, output/input characteristics, and non-idealities.

4.1.1 Voltage-Controlled Oscillators

Voltage-Controlled Oscillators (VCO) are components that create a single sinusoidal signal that oscillates at a specific frequency on the range $f_{min} \leq f_0 \leq f_{max}$, where the oscillation

frequency is fine-tuned by an externally applied DC voltage. VCOs may be used as local oscillators (LOs) in the mixing stage of an up- or down-converter in typical radar systems.

Solid-state oscillators convert DC voltages to sinusoidal steady-state RF waveforms using active non-linear devices. Low frequency oscillators may be designed using transistors with crystal resonators to provide frequency stability and retain low noise. Higher frequency sinusoidal RF waveforms may be achieved using transistors or diodes biased to a negative resistance with resonant, tank, circuits [41]. Additionally, using lower frequency oscillators in conjunction with frequency multipliers, higher frequencies—into the millimeter wave range—are achievable [42].

The typical block diagram of an oscillator may be modeled as a system operating with negative feedback, as shown in Figure 4-1.

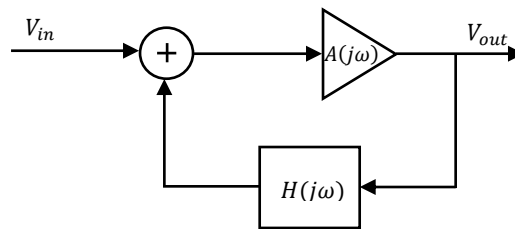


Figure 4-1: Block diagram of oscillator feedback network.

The output of this feedback system is given as

$$V_{out} = V_{in}A(j\omega) + V_{out}H(j\omega)A(j\omega) \quad (4.1)$$

which may be rearranged to take the form

$$V_{out} = \frac{V_{in}A(j\omega)}{1 - H(j\omega)A(j\omega)} \quad (4.2)$$

When the denominator of eq (4.2) approaches zero, oscillations will begin to occur at the frequency determined by the feedback network. Noting that a nonzero output voltage is possible for a zero input voltage. Accurate oscillation is actually a carefully tuned process that if done

incorrectly will cause chaotic rapid changes in amplitude at various frequencies other than the intended oscillation frequency.

Some of the most widely used feedback networks are the *Hartley*, *Colpitts*, and *Clapp* circuits. These are designed in FET circuits with common gate, common source, or common drain configurations. For more information on oscillator topologies, see [41] and [42].

4.1.2 Frequency Conversion Mixers

A mixer is a 3-port nonlinear device that uses diodes and transistors to preform up- or down- conversion of frequency components. While operating as an up-converter, the mixer takes an intermediate frequency (IF) signal and mixes it with a LO signal, creating higher radio frequency (RF) output signal components. If the LO signal is represented by the expression

$$v_{LO}(t) = \cos(2\pi f_{LO}t) \quad (4.3)$$

where f_{LO} is the frequency of oscillation and t is the time variable the, the up-conversion mixing process to the RF range may be described by

$$v_{RF}(t) = K v_{LO}(t) v_{IF}(t) \quad (4.4)$$

where $v_{IF}(t)$ corresponds to the IF signal voltage as a function of time and K is the conversion loss associated with the specific mixing device being used. The up-conversion process, as described in Figure 4-2 results in the spectral components following

$$f_{RF} = f_{LO} \pm f_{IF} \quad (4.5)$$

Where $f_{LO} + f_{IF}$ is known as the upper sideband (USB) and $f_{LO} - f_{IF}$ is known as the lower sideband (LSB). Typically, either the USB or LSB is then filtered out, leaving only one of the sidebands to be passed to the next piece of RF hardware. Choice of sideband is determined based on the desired frequency range of operation and RF hardware that is matched to correspond to this range.

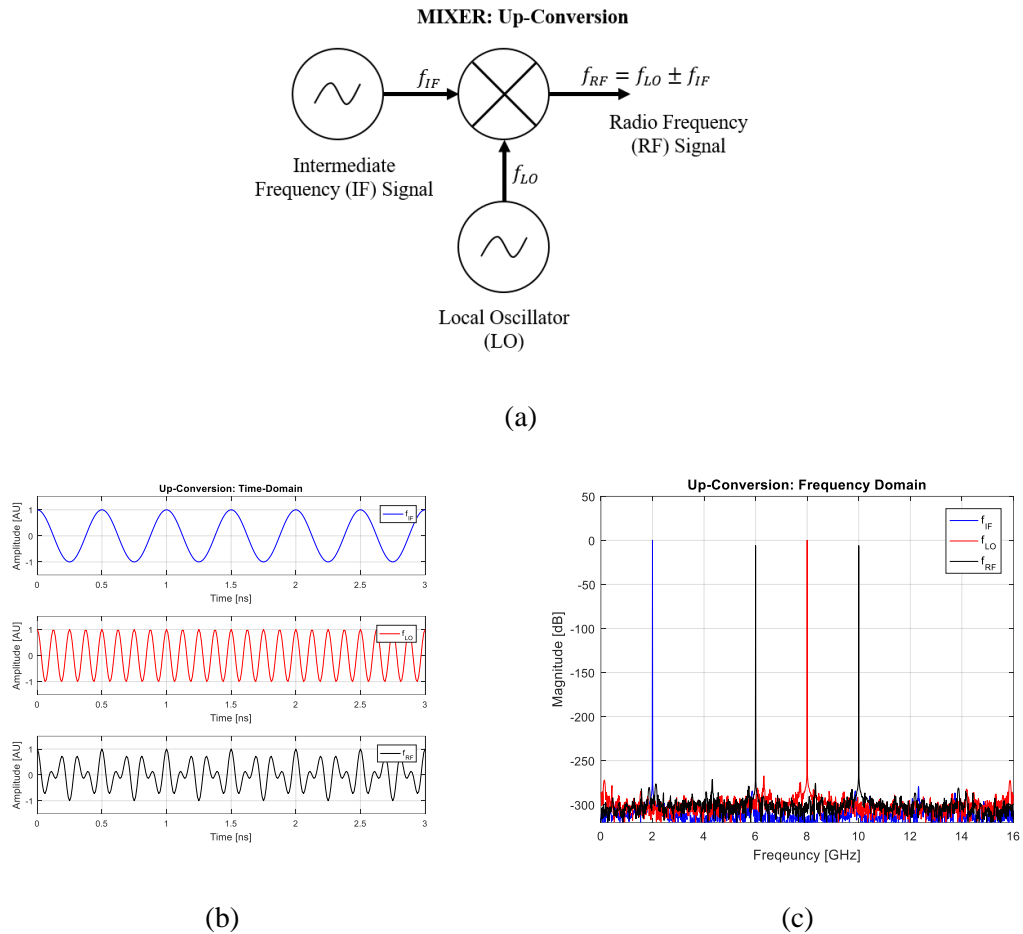


Figure 4-2: Frequency up-conversion using a mixer. (a) functional diagram (b) time-domain plots of each signal component and (c) associated spectral components of the up-conversion process.

Down-conversion follows a similar manner as up-conversion, but now the RF port serves as an input rather than an output. This process is described in Figure 4-3. Now the output returns the IF signal, which is described by the expression

$$v_{IF}(t) = K v_{RF}(t) v_{LO}(t) \quad (4.6)$$

again where K corresponds to the decrease in signal voltage due to conversion losses. Equation 4.6 now returns spectral components according to

$$f_{IF} = f_{RF} \pm f_{LO} \quad (4.7)$$

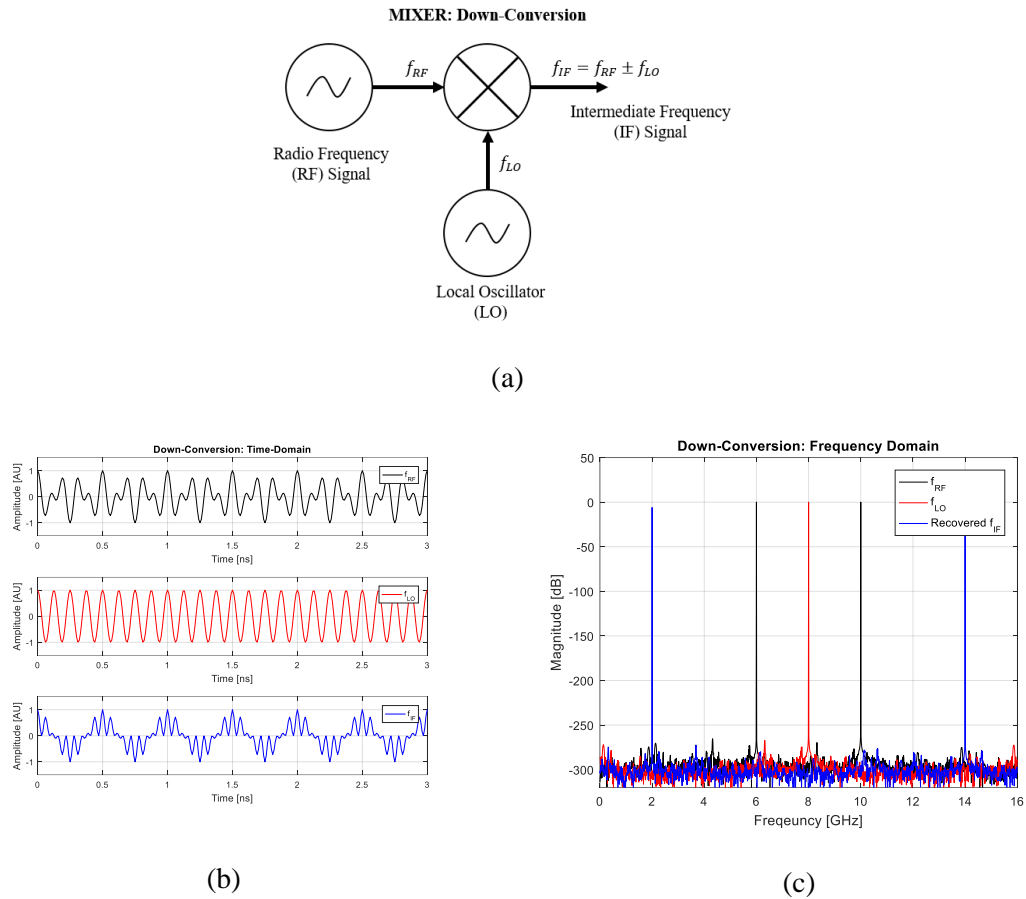


Figure 4-3: Frequency down-conversion using a mixer. (a) functional diagram (b) time-domain plots of each signal component and (c) associated spectral components of the down-conversion process.

where the desired output is the $f_{IF} = f_{RF} - f_{LO}$ component, which may be isolated simply through low-pass filtering.

An issue arises in the case that the RF signal present at the receiver input is equal to an *image frequency* given by

$$f_{IM} = f_{LO} - f_{IF} \quad (4.8)$$

Here, the output of the mixer will return a $-f_{IF}$ component, and due to symmetry of the Fourier spectrum for real-valued signals, the output will have an image response at the desired IF range—

leading to indistinguishable differences in the intended IF signals and the image. To avoid the introduction of this ambiguity, the RF signal should be filtered before the mixing conversion [41]. Other non-idealities for mixers to be taken into consideration are, port-to-port isolation, harmonics and combination products, linearity, intermodulation problems, noise figures, impedance and VSWR, and LO phase noise

4.1.3 RF Amplifiers

The purpose of an RF amplifier is to take a low powered input signal and output an amplified version, ideally without experiencing any nonlinearities. The amount of amplification is based on the gain parameter of the device and typically available in the associated datasheet. The gain is based on the basic input and output powers according to

$$G_{dB} = 10 \log_{10} \frac{P_{in}}{P_{out}} \quad (4.9)$$

Two common types of amplifiers used in RF design are power amplifiers (PAs) and low-noise amplifiers (LNAs). Generally, PAs are used to add a significant amount of gain before transmission via antenna and LNAs are used directly after a receiver antenna to amplify the signal and set the noise figure of the receiver (as seen in Chapter 2).

Amplifiers have what is known as a 1-dB compression point, which the output power level where the input/output relation is no longer linear. Hence, if the input to an amplifier is already at the amplifiers 1 dB compression point, the expected amplification will be significantly less than the listed gain on the devices datasheet.

Other notable parameters [43] are the gain flatness, which is the amount of variation from ideal gain over a specified frequency range (an example of this is shown in Figure 4-4; the harmonic distortion, which results in integral multiples of the input signal and is caused by the amplifier

operating non-linearly; the noise factor (discussed in section 2.2); and amount of return loss (RL), which is the ratio of the reflected power to that of the incident power at the input of the device.

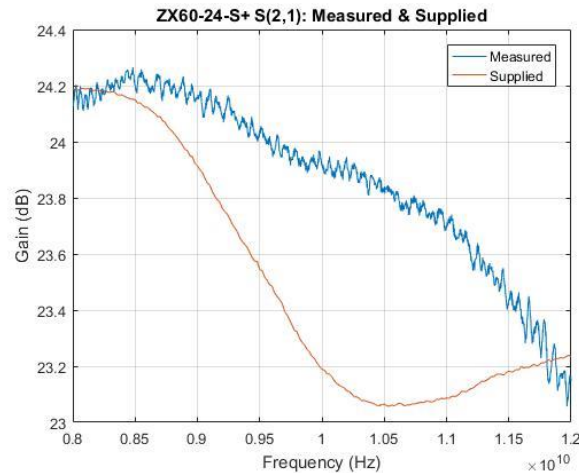


Figure 4-4: Amplifier gain characteristics (measured and supplied from manufacturer), listed as maintaining a high gain and flat response of $24 \text{ dB} \pm 1.3 \text{ dB}$ typ, over X-band frequency range.

4.1.4 UWB Horn Antennas

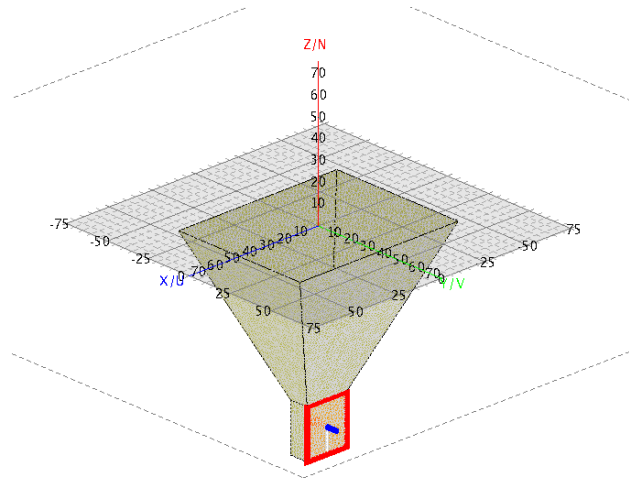
Ultrawideband antennas are designed to operate over a wide range of frequencies, while maintaining tolerable amounts of gain flatness. Horn antennas have been suggested that they are appropriate for NDT applications when operating in their near field regions [1, 44].

For through-wall human detection (TWHd) [31] found that, wider beamwidths ($\sim 100^\circ$) resulted in poorer results (more noise in range profile) and narrower beamwidths ($\sim 40^\circ$) resulted in clearer (distinct spike in range profile) and that if the gain of the antenna is greater than 6 dB, its beamwidth is less than 60° .

The UWB horn antennas used in this thesis are shown in Figure 4-5a and the simulated design in Figure 4-5b.



(a)



(b)

Figure 4-5: (a) One of two actual horn antennas used for NDT microwave imaging and (b) FEKO[®] simulation model.

The areas of electromagnetic fields around and antenna are divided between the near-field and far-field regions. The area near the aperture antenna can be further broken down into two regions: the reactive near-field and the radiating near-field. In the reactive near-field the relationship between the electric field and magnetic field are difficult to predict, allowing either to dominate at different points in space. The radiative near-field, also known as the Fresnel region is further away from the antennas, and therefore less influenced by the antennas self-capacitance, allowing for the electric and magnetic fields to become more predictable [45]. These regions are given by the distances in the following expressions [46].

$$\text{Reactive NearField: } R \leq 0.62 \sqrt{\frac{D^3}{\lambda}} \quad (4.10)$$

$$\text{Radiating NearField (Fresnel): } 0.62 \sqrt{\frac{D^3}{\lambda}} < R < \frac{2D^2}{\lambda} \quad (4.11)$$

$$\text{Far Field: } R \geq \frac{2D^2}{\lambda} \quad (4.12)$$

where D is the dimensions of the antenna (either length or diameter).

The width of the antennas used are 9.5 cm, and highest frequency of operation is 12.4 GHz, which leads the reactive near field to fall between the ranges of $11.67 \text{ cm} \leq R \leq 74.59 \text{ cm}$, and for 8.2 GHz the radiating near field lies between $0.489 \text{ cm} \leq R \leq 49.32 \text{ cm}$. These expectations are shown in the near-field simulations of the modeled horn antenna in Figure 4-6. For the results presented in this thesis, the chosen ranges of operation from a sample will lie within the radiating near field region (for 12.4 GHz).

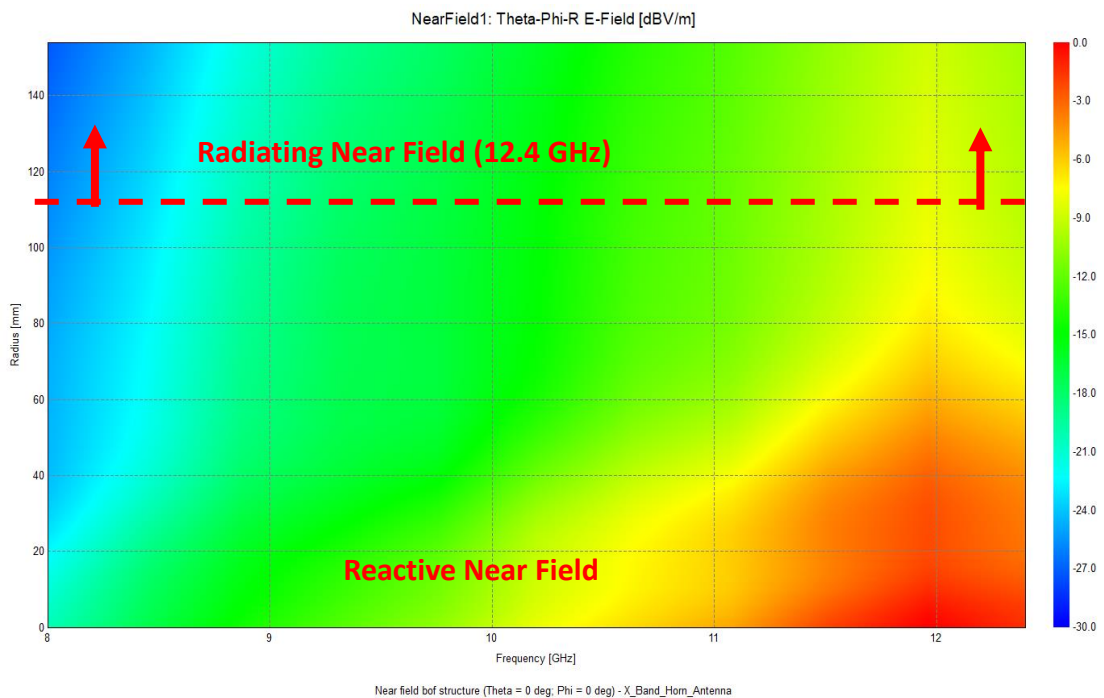


Figure 4-6: Near field simulation results of horn antenna in Figure 4-5.

4.2 System Description and Performance

The NDT imaging system is broken down into multiple blocks, as shown in Figure 4-7 and Figure 4-8, consisting of a host PC running MATLAB®; a Keysight M8190 arbitrary waveform generator (AWG) with 12-bit resolution at a sampling rate of 12 GSa/s; a dedicated X-band transmitter and receiver front end (RF signal chain), consisting of various low-cost components; an XY coordinate scanner, controlled by stepper motors running code on an Arduino microcontroller; and an Agilent Infiniium DSO90804A oscilloscope with 8 GHz of bandwidth and a sampling rate of up to 40 GSa/s.

The main script controlling the operation gathers the users input for the total scan dimensions in the x -direction (horizontal cross-range) and scan dimension in the y -direction (vertical cross-range), then any additional delay to be factored into the routine. The delay may be optimized to account for mechanical vibrations due to the physical structure moving. It is important

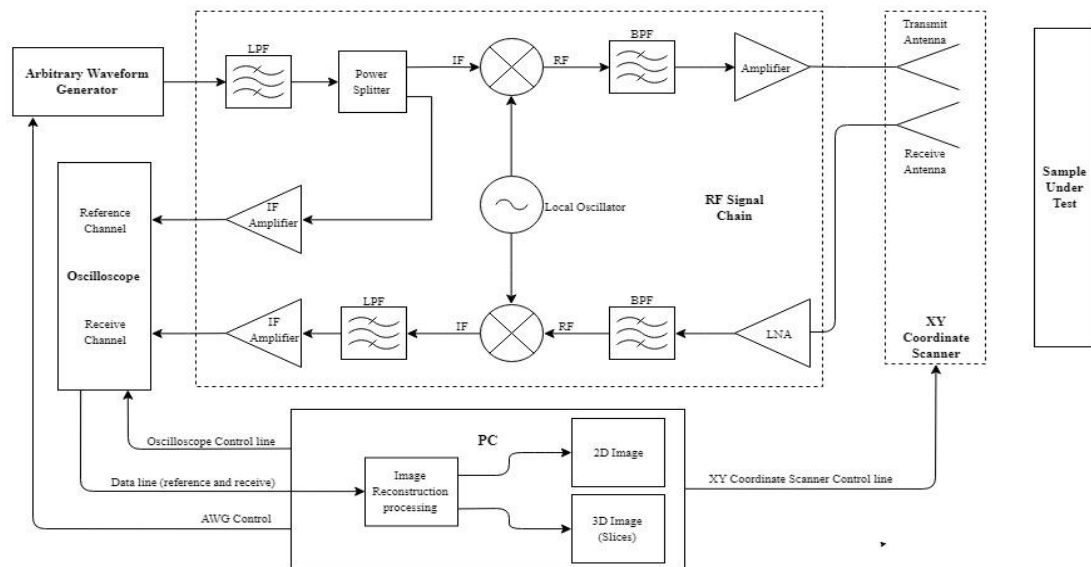


Figure 4-7: Block diagram of X-band microwave imaging radar system.

to make sure the carriage vibrations have dampened before taking measurements, or errors may arise.

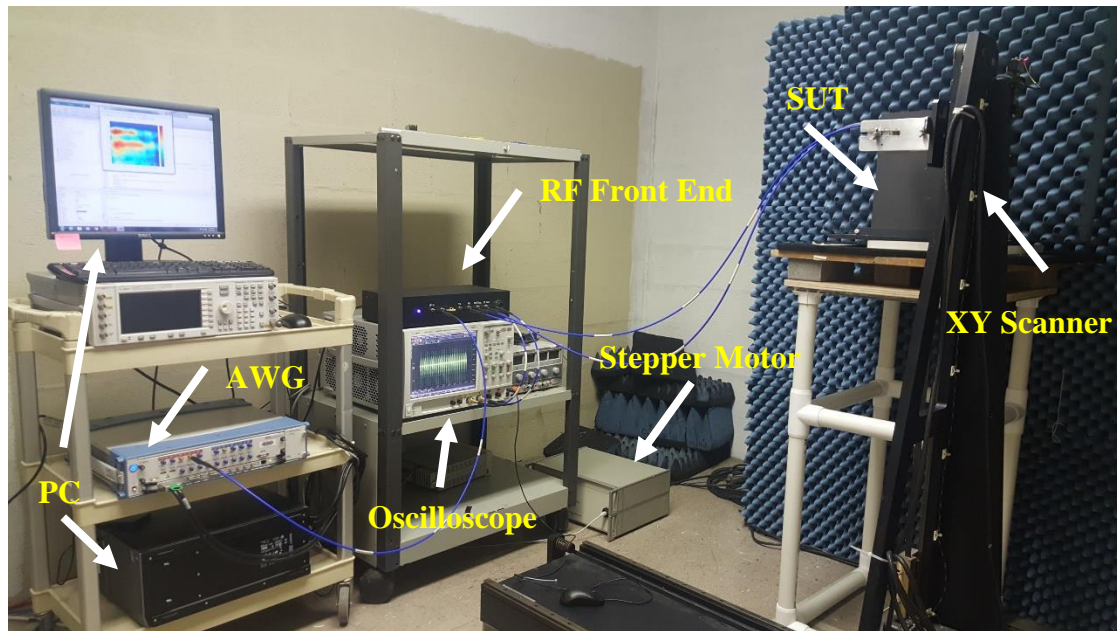


Figure 4-8: Main elements of non-destructive testing microwave imaging system.

The main steps of the PC's master routine are (1) transfer the intended waveform to the AWG (2) send a command telling the oscilloscope to sample the received (echo) and reference data channels, (3) transfer set of data via TCP/IP connection from the oscilloscope to the host computer, (4) apply the matched filter by operation of digital cross-correlation, (5) plot the peak value of the cross-correlation which relates to the total reflection coefficient, (6) send command to XY coordinate scanner to update the antenna positions, then repeat all steps until the complete dimensions of the scan region of covered.

The total sampling duration the oscilloscope measures data for (before clearing the buffer) at a single location is governed by the expression

$$T = \frac{N_{pts}}{f_s} \quad (4.13)$$

where N_{pts} is the total number of acquisition points and f_s is the sampling rate. As is the general assumption, the sampling rate must meet the Nyquist criterion of sampling at a minimum of two times the highest frequency in the signal being measured to avoid aliasing. The choice of T is dictated by the duration of the signal and the number of averages to be calculated.

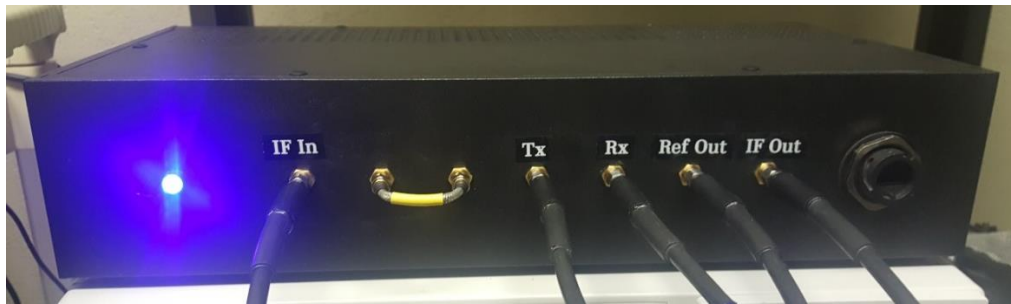
Once the data are gathered and the computer executes the matched filtering process in Matlab®, the data may be plotted using the following expression to define the down-range axis

$$R[n] = \frac{c * lag[z]}{2 * f_s * \sqrt{\epsilon_r}} - n_{delay} \quad z = 0, \pm 1, \pm 2, \dots \quad (4.14)$$

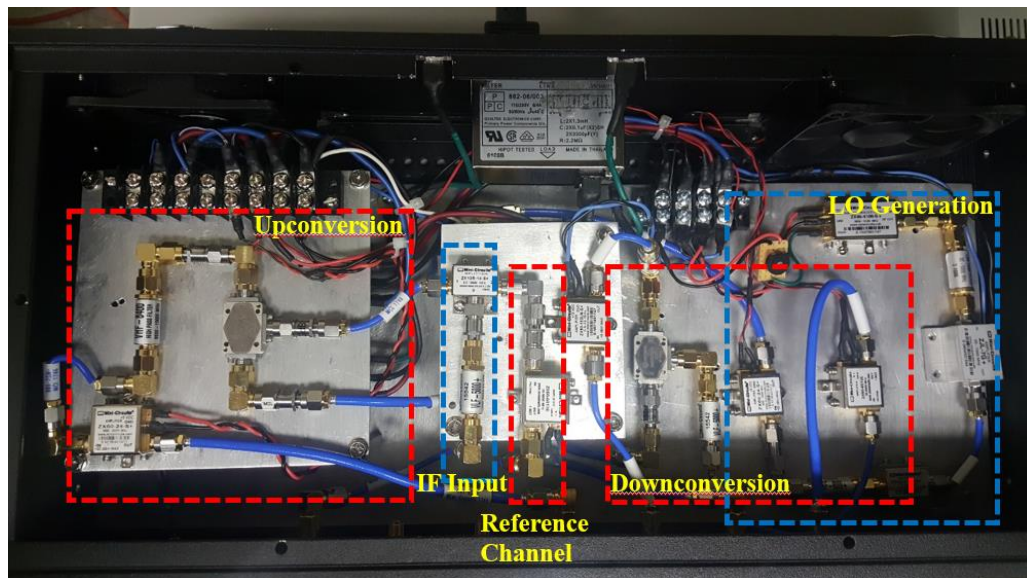
where R is the new range vector, $lag[z]$ is the vector created during the cross-correlation process, f_s is the acquisition sampling rate of the ADC, ϵ_r is the permittivity of the propagation media, and n_{delay} corresponds to the delay associated with the system (cables, components, etc.). The value of n_{delay} may be calibrated by setting a target at a known range and tuning the value of n_{delay} so the target appears at the proper range in the plotted range profiles.

4.2.1 System RF Front End

The main task of the RF front end (shown in Figure 4-9) is to take in the IF waveform (created in Matlab® and discussed in Chapter 3) from the AWG analog output, up-convert the signal to X-band, receive the reflected data, down-convert the signal back to IF, then route a reference (copy of the original transmitted signal) and the down-converted received signal to the ADC on the oscilloscope. The main sections of the system consists of an up-conversion section, a reference channel section, a down-conversion section, and a LO conditioning chain.



(a)



(b)

Figure 4-9: RF front-end (a) connection panel and (b) component layout views.

4.2.1.1 Up-conversion Signal Chain

The simulated block diagram for the up-conversion channel is shown in Figure 4-10. Here the AWG outputs a waveform at an IF range of roughly 0.5 – 4.5 GHz at 7.5 dBm, which is passed to the systems ‘IF In’ channel. The signal is then routed through a MiniCircuits VLF-5000+ low-pass filter (LPF) with a typical 3-dB cutoff of 5.580 GHz to remove any harmonics generated in the digital-to-analog conversion (DAC) process. The signal then travels through a 3-dB splitter to separate the intended transmission signal from a replica used for matched filtering. The IF signal (for transmission) is then mixed with an 8 GHz LO, which is up-converted to the RF range via a Miteq DM0812LW2 mixer with approximately 4.5 dB of conversion loss. The output of the mixer is then bandpass filtered (effectively using a high-pass filter) to isolate the USB using a MiniCircuits VHF-8400+ filter, with lower and upper 3-dB cutoff of 8.400 GHz and 13.00 GHz, respectively. To account for insertion, conversion, and other losses the now filtered RF signal is amplified using a MiniCircuits ZX-60-24-S+ ultrawideband RF amplifier with 24 dB of gain between 5 – 20 GHz. The ‘Tx’ output channel on the system chassis is then fed via coaxial cable to the SMA-waveguide adapter/horn setup mounted on the XY coordinate scanner carriage.

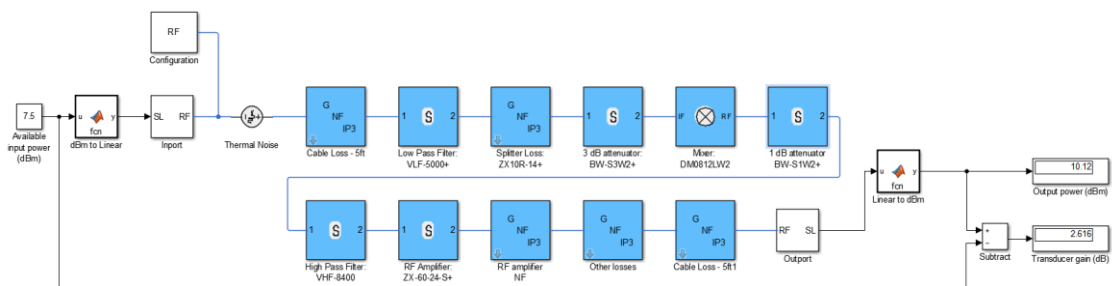
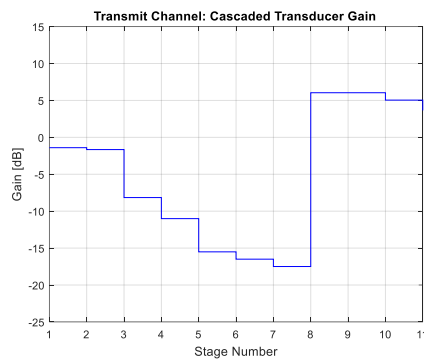
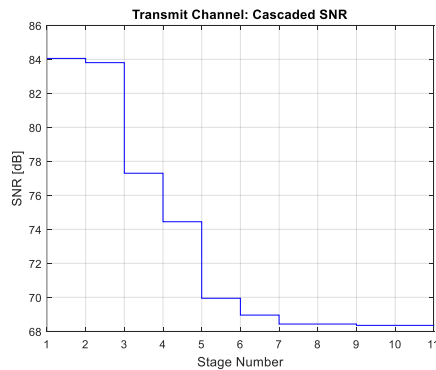


Figure 4-10: Simulink simulation of up-conversion block.

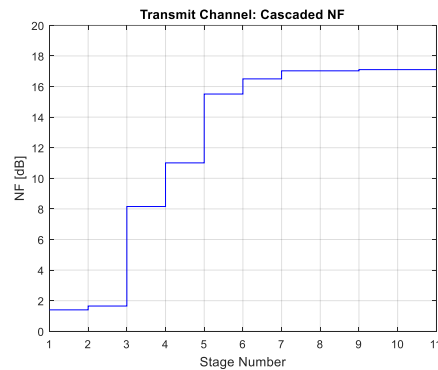
The simulated transducer gain, SNR, and NF of the cascaded up-conversion channel are shown in Figure 4-11. The simulated transducer gain (see appendix Appendix B) is found to be 3.16 dB and the output power of the RF front-end is found to be +10.12 dBm. This power is high enough to account for the high losses within various dielectrics, without driving the output power amplifier to its 1dB compression point and causing saturation.



(a)



(b)



(c)

Figure 4-11: Simulation results of the upconversion chain of the RF front end: (a) Transducer gain, (b) SNR and, (c) noise factor.

4.2.1.2 Down-conversion Signal Chain

The simulated block diagram for the down-conversion channel is shown in Figure 4-12. The input to this block is the reflected signal the receiving antenna captures. Immediately after the receiving antenna is a ZX60-153LN low-noise amplifier (LNA) with NF of 2.7 dB, which is placed here to maintain a high SNR/reduce the cascaded NF—as discussed in Chapter 2. After amplification, the signal is filtered through a VHF-6010 high-pass filter and routed through a Miteq DM0812LW2 with the same LO as the up-conversion stage to reduce phase errors. Once the signal is converted back to the IF range, the signal is filtered through a VLF-5000 low-pass filter, followed by a final stage of amplification through a ZX60-6013E amplifier, before being digitized by the ADC on the oscilloscope. The simulation results for this block are summarized in Figure 4-13. As can be seen, by using an LNA as the first component in the chain, we were able to maintain a high SNR, while adequately minimizing the cascaded NF (this is assuming $P_{received} = 0$ dBm).

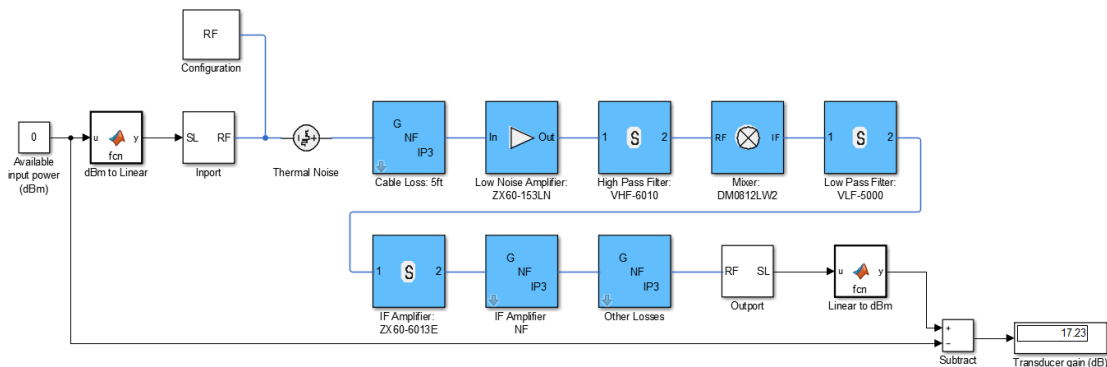
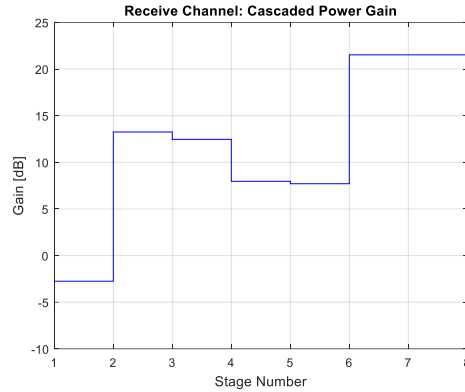
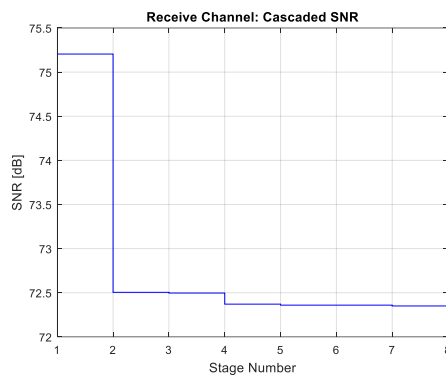


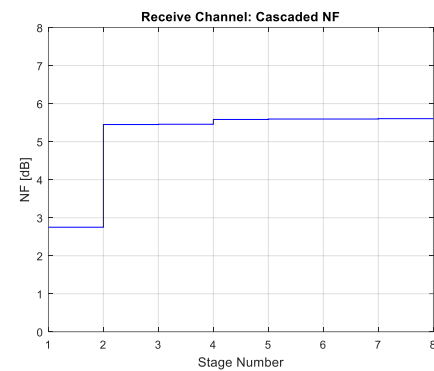
Figure 4-12: Simulink simulation of downconverter block.



(a)



(b)



(c)

Figure 4-13: Simulation results of the downconversion chain of the RF front end: (a) Transducer gain, (b) SNR and, (c) noise factor.

4.2.1.3 Reference Channel

The purpose of the reference channel is to create the signal that will be used in the matched filter operation with the received reflected data. The signal path for this chain is shown in Figure 4-14. The first blocks here are the same as for the up-conversion chain (block diagram shown in Figure 4-11). After the splitter, the signal is attenuated by 5dB to avoid any non-linearities from

occurring in the following IF amplifier. The main purpose of the amplifier is so that the signal experiences the same frequency characteristics of the same model IF amplifier used in the down-conversion channel.

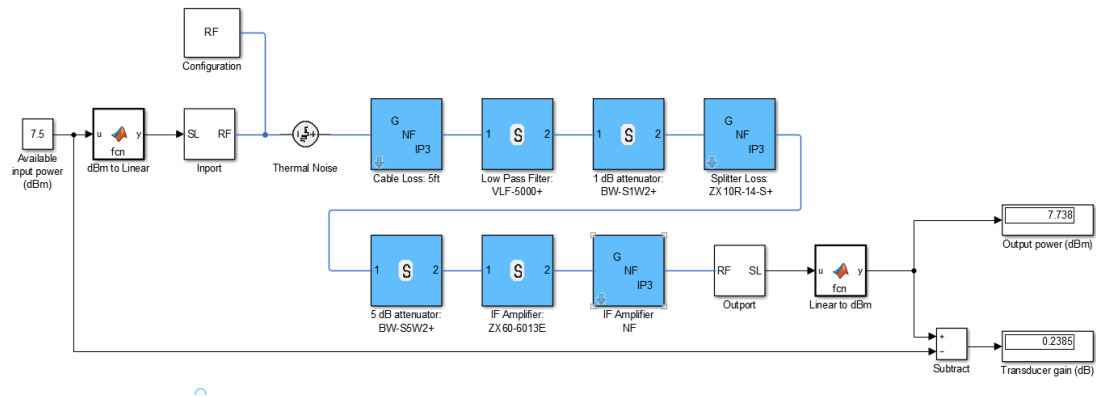


Figure 4-14: Simulink simulation of reference channel block.

4.2.1.4 Local Oscillator Generation Channel

The purpose of this block, which is shown in Figure 4-15, is to take a lower frequency 4 GHz VCO signal and convert it to a 8 GHz sinusoid to act of the LO for the up- and down-conversion processes. Here we take the output of the VCO, low pass filter it to remove any harmonics, then amplify the signal. The signal is amplified to the optimal input range of the 2x multiplier that converts the 4 GHz signal to 8 GHz. This multiplication process creates multiple harmonics that are then filtered through a bandpass filter—the signal is then reamplified through an RF amplifier. The output of the amplifier is driven beyond the 1dB compression point of the amplifier to achieve a higher power, but then must also be filtered again to remove any artifacts. The signal is then split to create the LO signal for both the up-conversion and down-conversion chains.

The power level requirement for the mixers are between +7 to +13 dBm. Taking into consideration other losses due to cables, connectors, non-idealities, the output power of the LO approximately +10 dBm. The simulated results are shown in Figure 4-16.

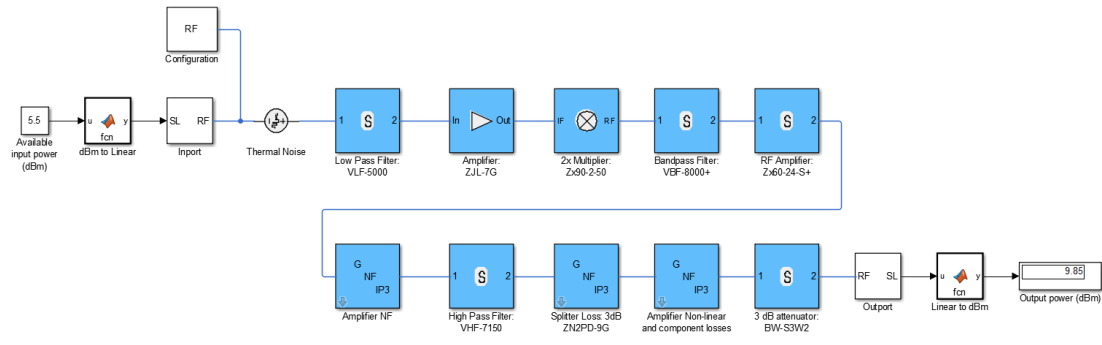


Figure 4-15: Block diagram of LO conditioning channel used for mixing stages, with noise figures and amplifier non-linearities accounted for.

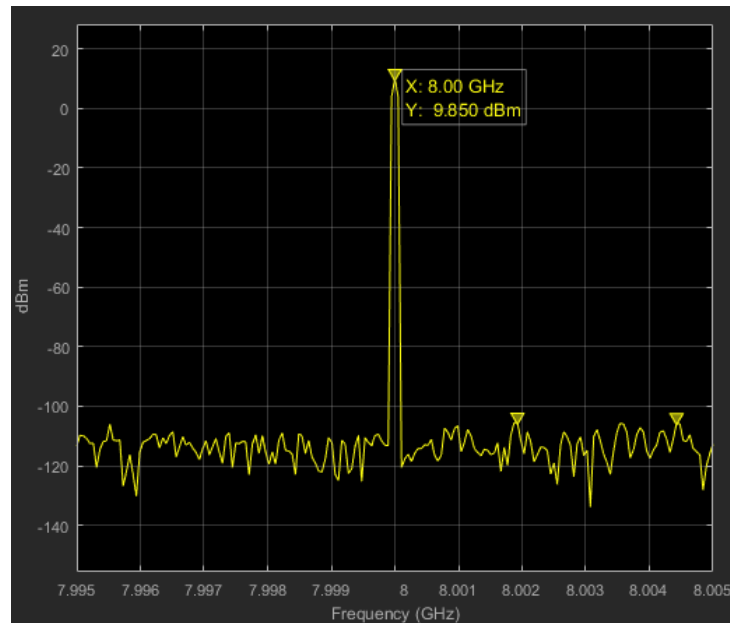


Figure 4-16: Simulated output of LO channel.

Chapter 5 System Validation and Experimental Results

This chapter demonstrates the abilities of the X-band NDT microwave imaging system—using UWB noise pulses—through a series of A-scans (one-dimensional measurements), B-scans (two-dimensional measurements), and C-scans (three-dimensional measurements). Initially, we discuss a method for choosing optimal stand-off distances between the antennas and the samples under test. We then look at the cases of highly reflective cylindrical targets at chosen distances from the antennas and the system’s ability to resolve them when spaced closely together. Next we look at the system’s ability to detect a hidden water inclusion sandwiched in-between the layers of a dielectric polyvinyl chloride (PVC) sample. Following tests pertain to the concepts discussed in Chapter 1, with the goal of detecting anomalies such as air voids in structures reinforced with composite materials, detecting the presence of $\text{Al}(\text{OH})_3$ —to simulate the effects of galvanic corrosion—in hybrid composite materials, and determining if delaminations have occurred in CFRP samples subject to impact damages from hand tools.

For the extent of this chapter, the notations shown in Table 5-1 will be assumed for all measured or calculated signals. The matched filter of the received signal and reference signal will be conducted using the cross-correlation technique described in Chapter 2 to arrive at the impulse response of the system under test. The operation parameters as shown in Table 5-2 are assumed to remain constant for all tests unless noted otherwise. Additionally, all images have a degree of interpolation done to them using Matlabs® *interp2* function.

Table 5-1: Summary of Testing Variables

Table 5-1: Summary of Testing Variables	
Transmitted Signal	$s_t(t)$
Received Signal	$s_r(\hat{t})$
Reference Signal	$s_{ref}(\hat{t})$
Digitized Received Signal	$s_r[n]$
Digitized Reference Signal	$s_{ref}[n]$
Digital Output of Matched Filter operation	$s_d[n]$

Table 5-2: Constant System Parameters

Table 5-2: Constant System Parameters	
Parameter	Value
Waveform generation sampling rate	12 GSa/s
Signal Bandwidth	4 GHz
IF range (before up conversion)	0.5 – 4.5 GHz
Local Oscillator frequency	8 GHz
RF range (after up conversion)	8.5 – 12.5 GHz
Output Power	+10 dBm
Pulse Duration (noise pulses)	2.5 ns
Pulse Repetition Interval (PRI)	10 ns
Coherent Integrations	27

5.1 Testing Requirements for Near-Field Imaging

5.1.1 Standoff distance Optimization Method

When working in the near-field of the antennas aperture, the EM fields radiated from the antennas do not follow the far-field characteristics of the antennas. Therefore, it is an important to understand how a certain sample-under-test (SUT) will react to the fields incident upon it, and how the sample itself will interact with the impedance of the antennas. The method (similar to [1]) used throughout this thesis is based on the following stand-off distance range optimization approach:

- i. With the SUT almost in-contact with the antenna apertures, measure the voltage peak-to peak, $V_{no\ target}^{pp}$, of the reflected pulses with no target placed behind the SUT.
- ii. With the SUT at the same stand-off distance, place a highly reflective target directly behind the sample, and again, measure the voltage peak-to-peak, V_{target}^{pp} , of the reflected pulses.
- iii. Move the SUT a distance of Δz further from the antenna apertures and repeat steps i and ii.
- iv. Repeat steps i-iii until a sufficient number of stand-off distance ranges have been investigated.
- v. Calculate the voltage differences for each range at which measurements were taken, by

$$\Delta V_{pp}[z] = |V_{no\ target}^{pp}[z] - V_{target}^{pp}[z]| \quad (5.1)$$

The optimization method will show peaks in the difference graph (equation 5.1), which are the ideal stand-off distances for the *specific* SUT that the tests were done for. This method needs to be conducted whenever a new type of SUT is being used.

As an example, the aforementioned method was conducted for an 8-ply unidirectional CFRP panel at ranges between 2 cm – 20 cm, with $\Delta z = 1$ cm, and the reflective target used for the “with target” cases was a PEC block. Figure 5-1a shows the raw voltage peak-to-peak data for both cases (with and without the PEC target behind the SUT), while Figure 5-1b shows the application equation 5.1. From (b) we can see the locations circled in red are the optimal stand-off distances specifically for this type of sample—4, 9, 12, and 16 cm.

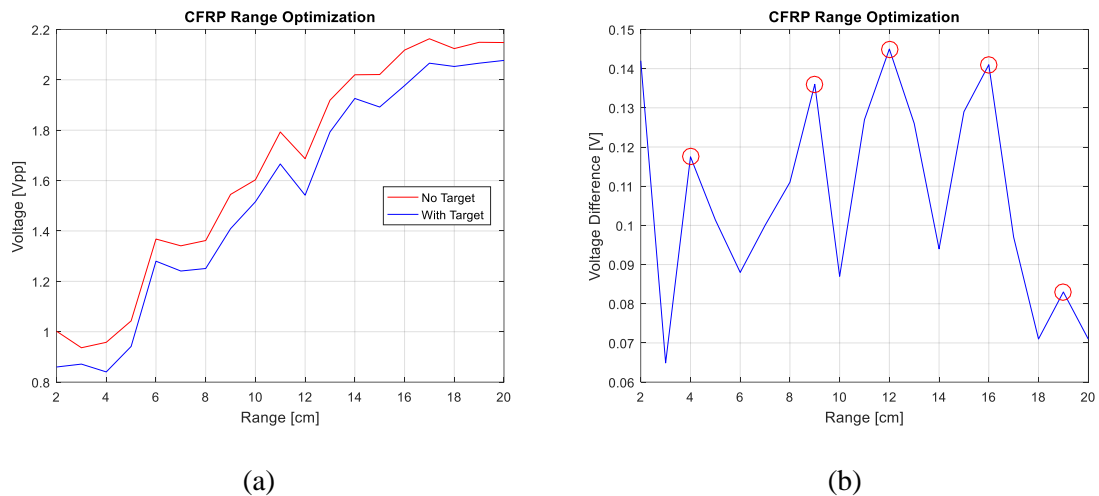


Figure 5-1: Range optimization tests for CFRP panel. (a) Raw voltage peak-to-peak data for cases of with and without target behind sample and (b) the voltage differences at each range.

5.1.2 Sampling Coherence of Reflected Data

Phase coherence of pulses at each sampling position is critical for accurate averaging and reconstruction of 2D or 3D images. If coherence is not maintained, then the migrated images will have misaligned ranges. For example, imagine that we have two point targets, each located at a down-range distance R_0 from the antenna apertures and equally spaced in cross-range direction. Under these conditions, and assuming coherence between data collection of reflected data at each sampling location, the migrated image will show the presence of the two targets at the same range. Now assume, sampling coherence was not maintained, then one of the targets (keeping in mind both are placed at a range R_0 from the antennas) will erroneously appear to be in front or behind the other target.

5.2 System Validation Measurements

5.2.1 A-Scan Target Ranging Tests of Cylindrical PEC Targets

To validate the theoretical range-resolution, consider the case with two PEC cylindrical targets placed down range from the antenna apertures, as shown in Figure 5-2. Assuming the PEC cylinder closest to the antennas is held at a constant range of 13 cm and the second is dynamic and moved closer to the target for subsequent tests, each target should be individually distinguishable until their separation is less than the theoretical range resolution. If the waveform used for the tests is the noise pulse as discussed in section 3.1.3 with a bandwidth of 4 GHz, it is assumed that for an in free-space measurement we should expect a theoretical range resolution of approximately 3.75 cm. To be noted, that this is the ideal range-resolution, and the non-ideal effects of multipath and waveform sidelobes may potentially impact the results.

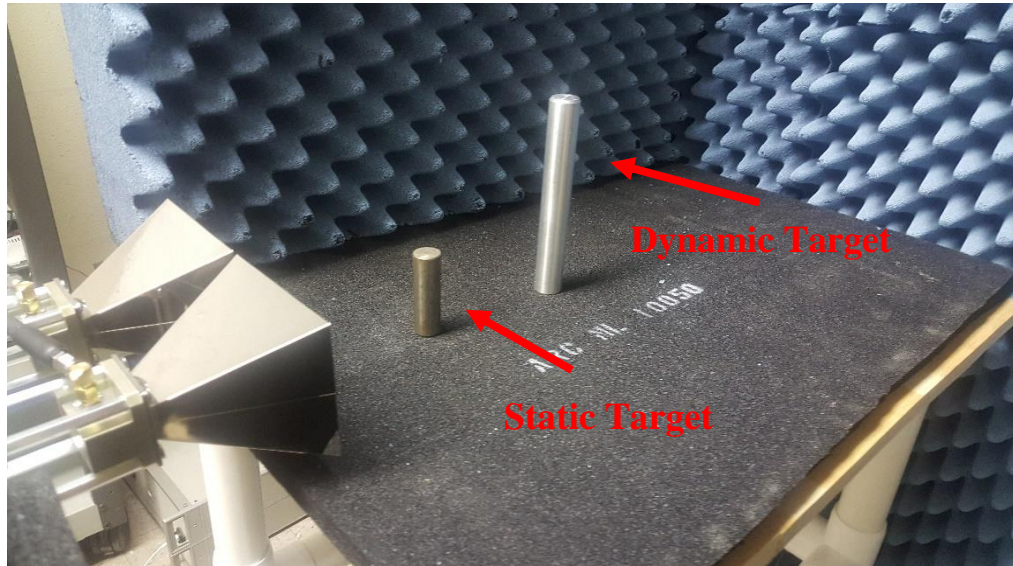


Figure 5-2: Measurement setup for range-resolution validation tests.

Initially the two targets are placed at 20 cm apart on a broadband multilayer absorber with a return loss of roughly -20 dB over the X-band range [47]. A single A-scan is conducted to give a 1D range profile as shown in Figure 5-3a. Figures 5-3b-d show the target separation at 10 cm, 3.75 cm (theoretical range resolution), and 2.5 cm.

The range profiles show that for separation distances greater than the theoretical range resolution, the targets appear as distinctly separate objects—but when the separation is less than 3.75 cm (for the case of freespace and $B = 4$ GHz) the targets appear as one. Based on these results, it is reassuring to confirm that the system is producing expected results.

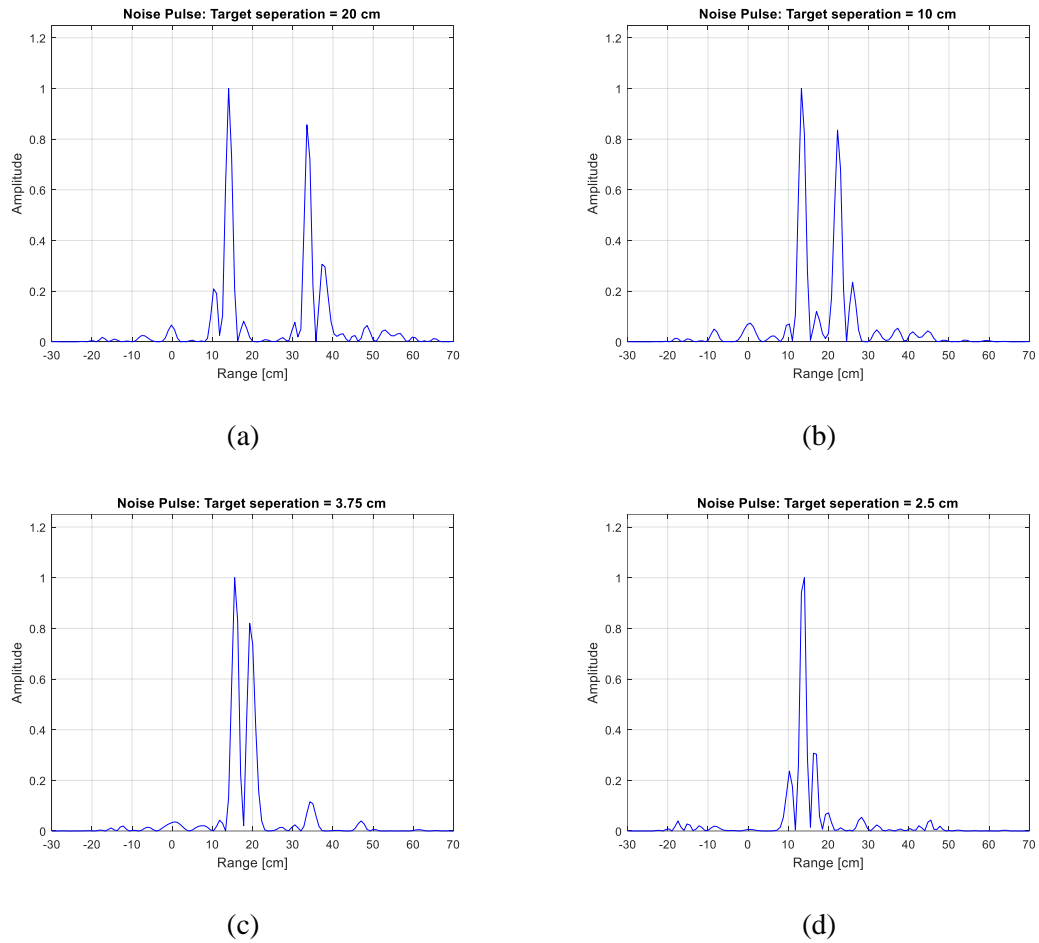


Figure 5-3: Range profiles of two cylindrical PEC targets separated by (a) 20 cm (b) 10 cm (c) 3.75 cm and (d) 2.5 cm.

5.2.2 B-scans of Single and Multiple Cylindrical Objects

Next, two-dimensional B-scans were run for two cases: (i) single cylindrical PEC target and (ii) one wooden and two PEC cylindrical targets. The associated geometry is shown in Figure 5-4, where the range from the antennas to the point target at any given point along the scan axis is

$$R = \sqrt{(x_0 - x)^2 + (R_0)^2} \quad (5.2)$$

where R_0 is the chosen stand-off distance. If $s_t(t)$ is radiated downrange towards the target, the received signal may then be expressed as

$$s_r(t) = \sum_{n=1}^N a_n \cdot s_t(t - \tau) \quad (5.3)$$

where a_n is an attenuation constant based on the reflectivity of the N -th point source within the illuminated scene, as well other propagation losses. Here the variable τ represent the path delay between the receiving antenna and the scattering object. In general the amount of delay is given by

$$\tau = \frac{2R}{c} \quad (5.4)$$

where $c = 2.9979 \cdot 10^8 \left[\frac{m}{s} \right]$ is the speed of light and R is the distance from the antennas to the scattering object.

Figure 5-5a-c shows the motion of the antennas for case i with respect to a single target placed at 13 cm from the antennas. The results of the B-scan are shown Figure 5-5d, where based

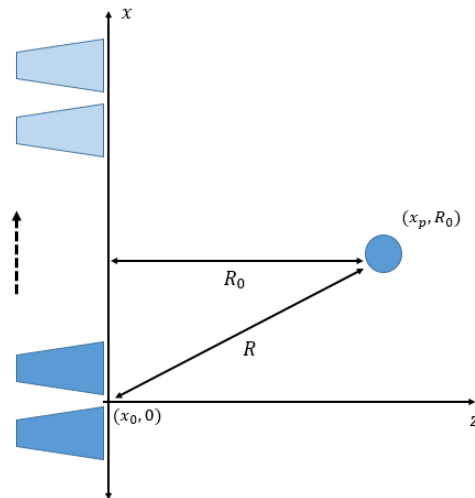
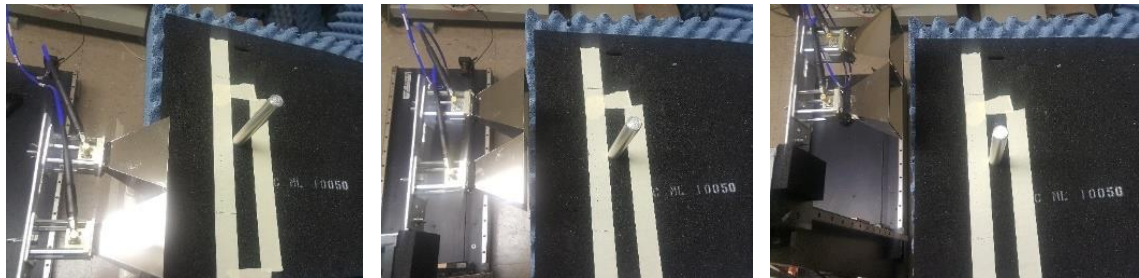


Figure 5-4: System coordinates for a 2-D scan.

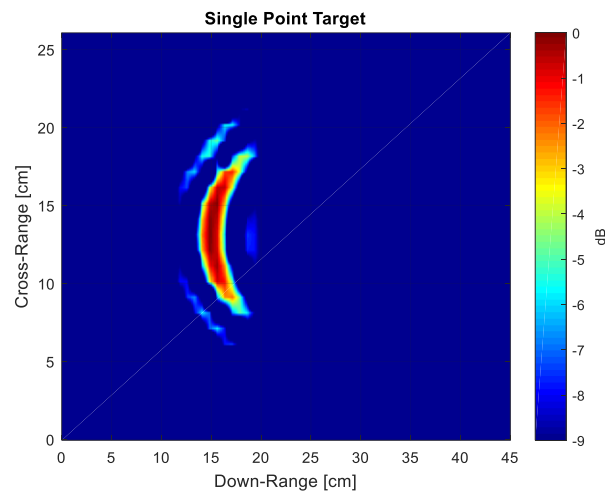
on the different propagation times of the reflected signal at various locations, the results appear as a hyperbolic shape.



(a)

(b)

(c)



(d)

Figure 5-5: (a-c) Scanning path of antennas for B-scan of single cylindrical PEC target and (d) results

For case ii, the signal and system parameters (waveform, bandwidth, output power) remain constant, but now the test is conducted for the case of arbitrarily placed targets around the imaging scene—a cylindrical wooden target at (17cm, 14cm), and two cylindrical PEC targets at (33 cm, 14 cm) and (32 cm, 23 cm). Following the B-scan, the reconstructed space-time image is reconstructed

and shown in Figure 5-6. All the targets are detectable, but due to locations of coherency of multipath signals, false ghost images are also visible surrounding the locations of the actual targets.

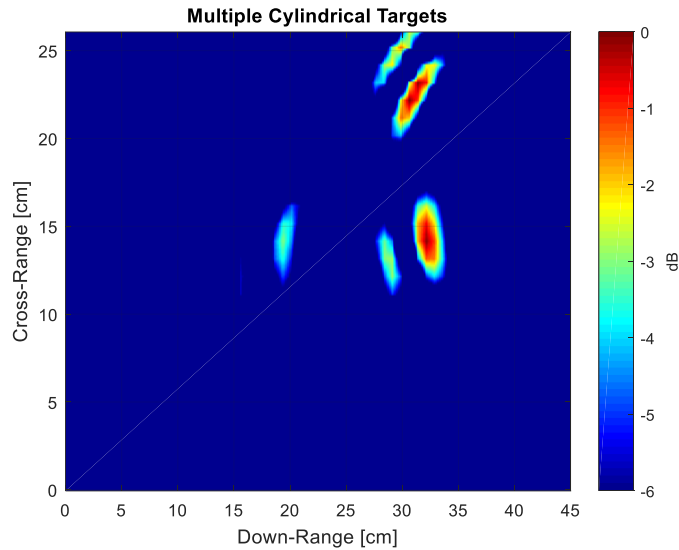


Figure 5-6: B-scan results of 3 targets (wooden rod and two cylindrical PECs)

5.2.3 C-scans of Polyvinyl Chloride (PVC) Sample with Water Inclusion

In this section, we now expand the system operation to a three-dimensional (3D) C-scan. The antennas will cover a 2D plane, capturing individual A-scans at each step, yielding an $M \times N$ group of range profiles (A-scans). The datum collected at one discrete sampling location corresponds to the highlighted boxes shown in Figure 5-7. The data may also be interpreted as multiple B-scan slice planes, which will be shown in the results.

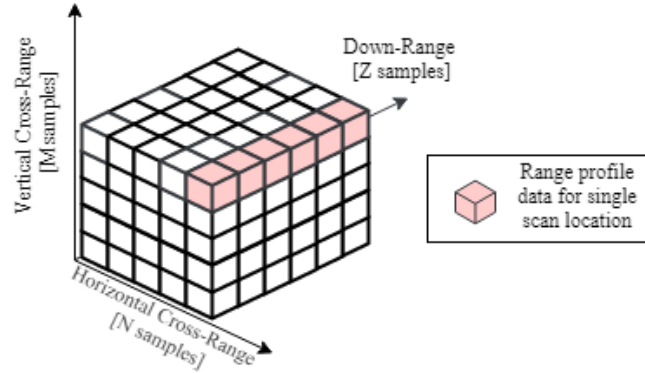


Figure 5-7: Data organization scheme (for arbitrary $5 \times 5 \times 6$ set of data), where colored boxes represents data gathered at one sampling location or a single A-scan.

Now we create a multilayer dielectric sample using two sheets of polyvinyl chloride (PVC). A highly reflective water sample (in a $4.5 \text{ cm} \times 4.0 \text{ cm}$ Ziploc[®] bag) is placed in a small prepared cavity of one of the PVC samples as shown in Figure 5-8. With the water inclusion placed in the

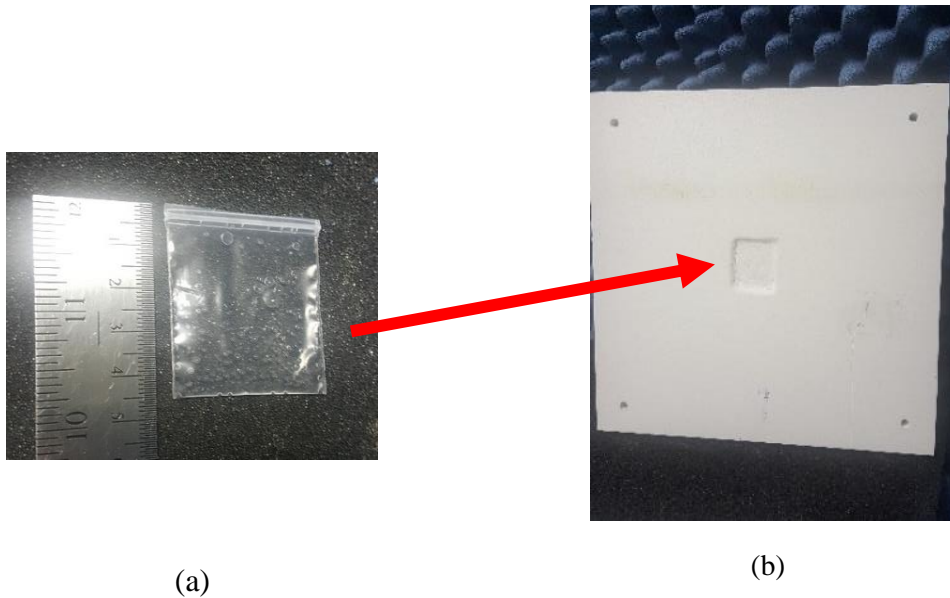
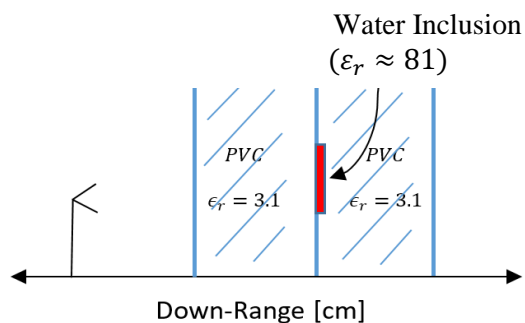


Figure 5-8: (a) Water inclusion placed in cavity (b) of PVC sample.

cavity, the second PVC sample is connected to the face of the first PVC sample, hiding the water inclusion from the human eye, as depicted in Figure 5-9. Each PVC panel is 2-cm thick, leading to a sample of total thickness of 4 cm.



(a)



(b)

Figure 5-9: Measurement geometry (a) of PVC sample with hidden water inclusion (b) between layers.

The range from the antennas to the front face of the PVC sample was set to $R = 14$ cm, while the receiver spacing sampling interval in the horizontal and vertical cross-range directions was set to be $\Delta x = \Delta y = 1.016$ cm (0.4 in), with $M = N = 16$. All other parameters are shown in Table 5-1. The orientation of the antennas with respect the PVC sample are shown in Figure 5-10.



Figure 5-10: Antenna orientation with respect to PVC sample with hidden water inclusion

As stated at the start of this section, the 3D C-scans will be represented by a collection of B-scan slices. Figure 5-11 summarizes how this orientation works. The parameters for these tests are restated in Table 5-3.

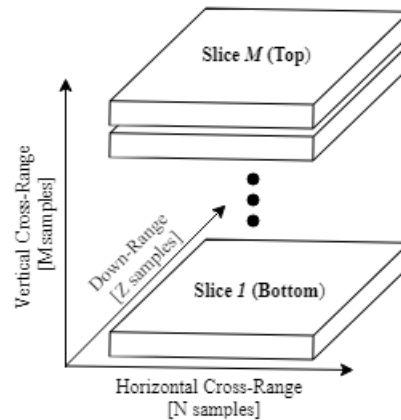


Figure 5-11: Geometry which shows range definition and orientation of slices for viewing 3 dimensional data sets.

Table 5-3: Parameters for Multilayer PVC with Water Inclusion C-scans	
Sample	Multilayer PVC sample
Scenario	Hidden water inclusion
Waveforms tested	GMSP, Noise Pulse w/ high PSLR, Noise Pulse w/ low PSLR
Standoff Distance	$R_0 = 14$ cm
Scan Dimensions	20.32cm \times 20.32 cm
Cross-range sampling interval (both vertical and horizontal)	1.016 cm

The results of the C-scan while using a GMSP, noise pulse with a high PSLR, and noise pulse with a low PSLR are shown in Figures 5-12, 5-13, and 5-14, respectively. The main observation is that the water boundaries and the water inclusion are easily detectable for the cases of the GMSP and noise pulse with high PSLR. In the case of the noise pulse with a low PSLR, the presence of a foreign object is visible, but discrete boundaries are near impossible to detect, further suggesting that the noise waveform needs to be tailored for use in near-field imaging.

In comparison of the results for the GMSP and noise pulse with high PSLR waveforms, the images suggest that the noise pulse outperforms the GMSP at identifying the outer boundaries of the PVC sample, which are most noticeable in the top slices. In addition, the noise pulse results reflect the actual width of the water sample more accurately, especially at the upper and lower extremes.

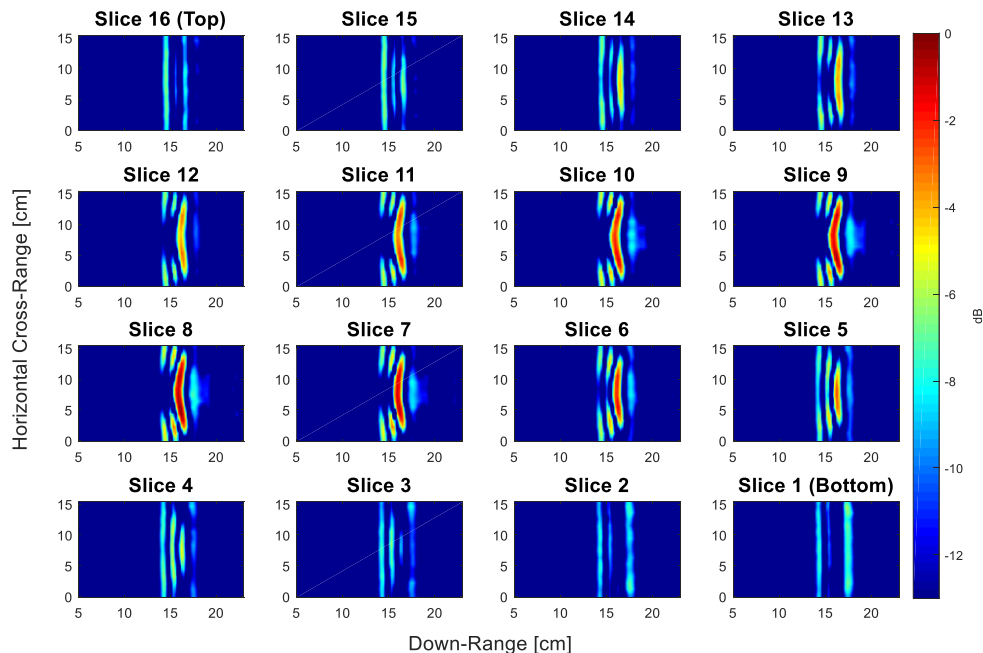


Figure 5-12: C-scan results a PVC sample using GMSP.

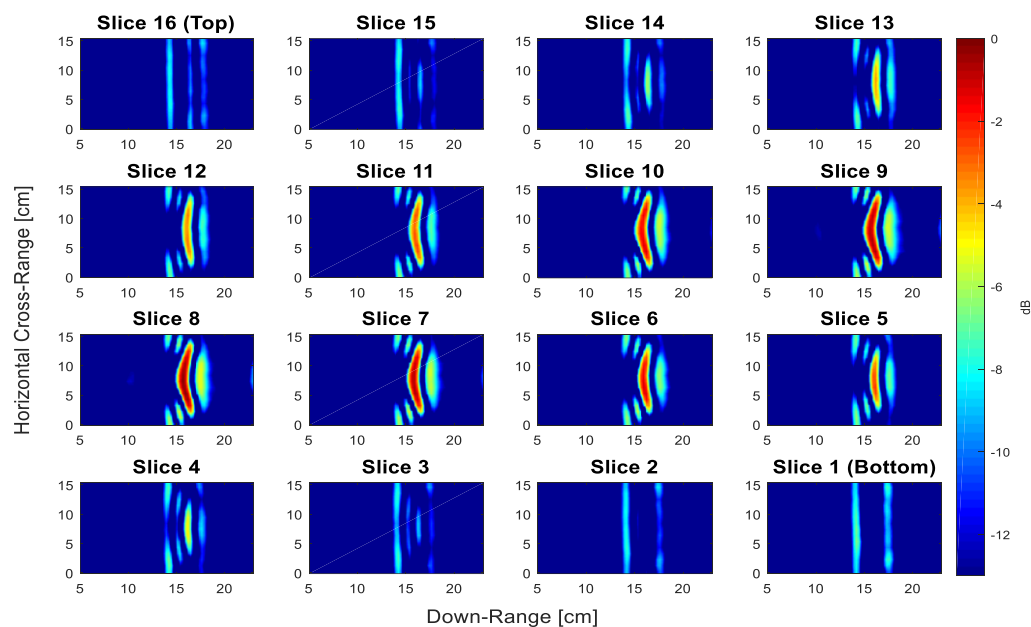


Figure 5-13: C-scan results a PVC sample using noise pulse with high PSLR.

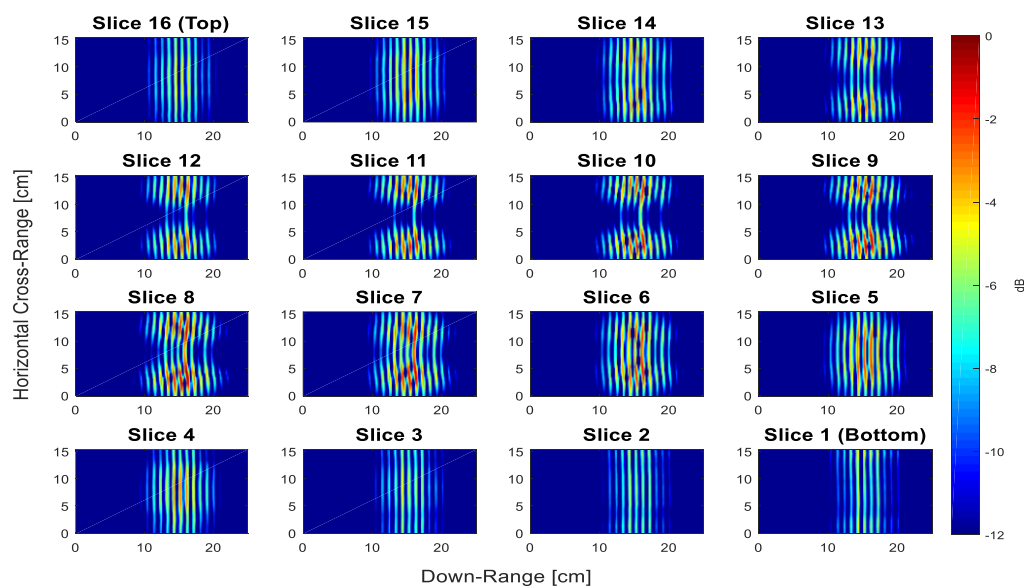


Figure 5-14: C-scan results a PVC sample using noise pulse with low PSLR.

5.3 Composite Material Experiments

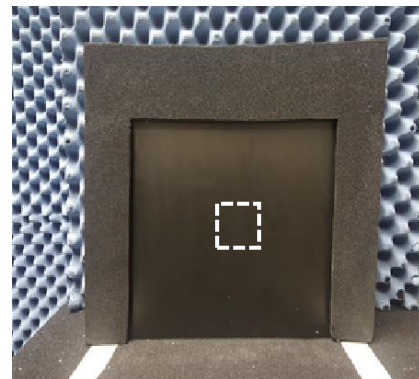
The results presented in this section are created by conducting C-scans across the samples under test and extracting the peak value of the cross-correlation operation, which are then plotted as the associated pixel value in a two-dimensional image.

5.3.1 GFRP Reinforced Cement Hybrid Wall with Air Void

The main wall structure was made using concrete bricks and set using a quick drying mortar, as shown in Figure 5-15a. A glass fiber reinforced polymer (GFRP) is attached to the front face of the concrete wall using a heavy duty adhesive, as shown in Figure 5-15b. A small air void was introduced into the sample in the location of the shaded 5 cm \times 5 cm shaded region in Figure 5-15a, by not applying adhesive to this area, before attaching the GFRP sample.



(a)



(b)

Figure 5-15: Concrete wall before adhering GFRP panel (a) where shaded region represents area where no adhesion is to be applied, which results in air gap between concrete and GFRP boundary. (b) Completed concrete/GFRP wall in place for C-scan trials, with the white outline representing location of air void (bonding defect).

The parameters for the following C-scans are given in Table 5-4 and all other parameters are given in Table 5-2. The orientation of the antennas with respect to the GFRP/cement hybrid sample are shown in Figure 5-16.

Table 5-4: Testing Parameters for GFRP/Cement Hybrid Wall C-scans	
Sample:	GFRP reinforced concrete wall
Scenario	Air void (~ 5 cm × 5 cm)
Waveforms tested	GMSP, Noise Pulse
Standoff Distance	$R_0 = 16$ cm
Scan Dimensions	20.32cm × 20.32 cm
Cross-range sampling interval (both vertical and horizontal)	1.016 cm

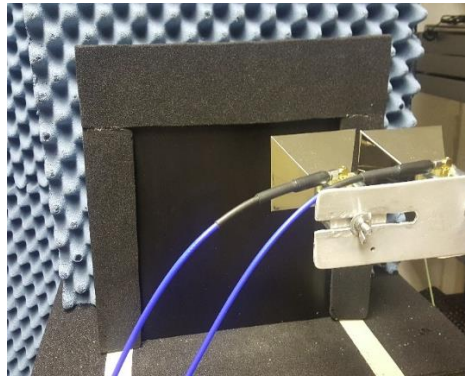
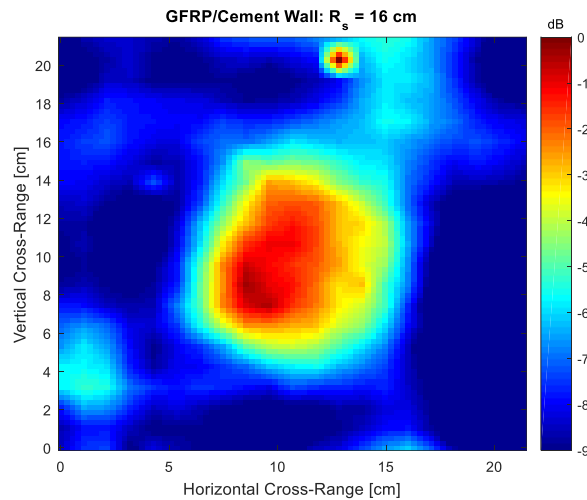


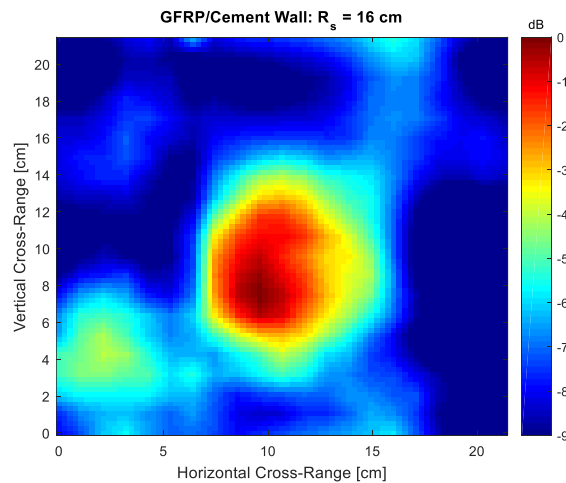
Figure 5-16: Measurement setup for detection of air void in GFRP/concrete wall structure.

The results are presented in Figure 5-17. Here, again, each pixel value corresponds to the peak value of the correlation operation, which are relative to the total input reflection coefficient. The results show that the presence of the air void is detectable, even for void thicknesses less than the theoretical range resolution given by equation (2.6), for both waveforms. Additionally, the

mortar layers between the concrete bricks are also distinguishable using this method. One notable difference in the results are that the reconstructed image using the noise pulse yields a more accurate representation of the actual size of the air void and the detection of an unexpected air void in the lower left due to non-uniformities in the construction of the cement wall.



(a)



(b)

Figure 5-17: C-scan results of GFRP/cement wall hybrid using (a) GMSP and using (b) noise pulse.

5.3.2 Galvanic Corrosion of CFRP/Aluminum Hybrid Composite

To test for the presence of the $\text{Al}(\text{OH})_3$ in a composite hybrid material, the sample depicted in Figure 5-18 was developed to model the onset of the galvanic corrosion effects. Here, a small 5.0 cm \times 6.0 cm cavity was created to house a sample of the $\text{Al}(\text{OH})_3$, which was placed in a 4.0 cm \times 4.5 cm Ziploc[®] bag. A 30.48 cm \times 30.48 cm 6-ply unidirectional CFRP panel was then coupled to the face of the metal backing plate

Two scenarios were measured by the noise based NDT imaging system: (1) Without the $\text{Al}(\text{OH})_3$ present and (2) with the $\text{Al}(\text{OH})_3$ present. To remain consistent and reduce the influence of the Ziploc[®] bag, for the test without the $\text{Al}(\text{OH})_3$ an empty bag was placed in the cavity to account for any variation specifically due to the bag.

The tests were conducted according to the parameters given in Table 5-5. The results for the case of no $\text{Al}(\text{OH})_3$ in the cavity are shown in Figure 5-19a and for with $\text{Al}(\text{OH})_3$ in the cavity in Figure 5-19b.

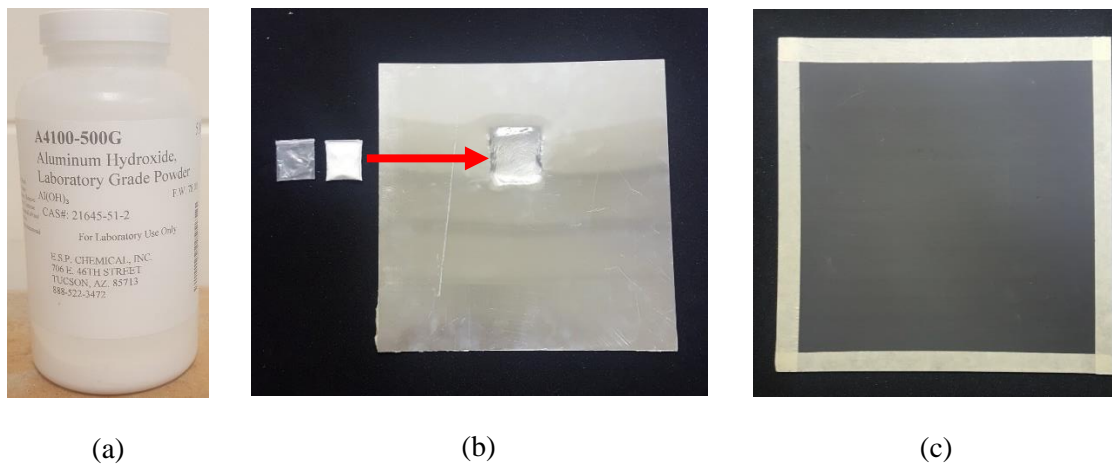
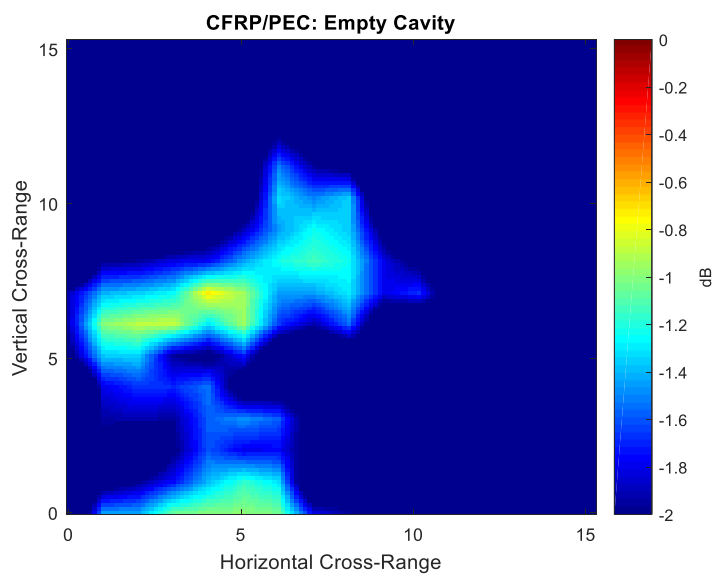


Figure 5-18: Sample preparation for corrosion measurement tests. (a) Laboratory grade $\text{Al}(\text{OH})_3$ powder (b) Metal backing plate with cavity and $\text{Al}(\text{OH})_3$ sample; (c) CFRP panel coupled to front of metal backing plate.

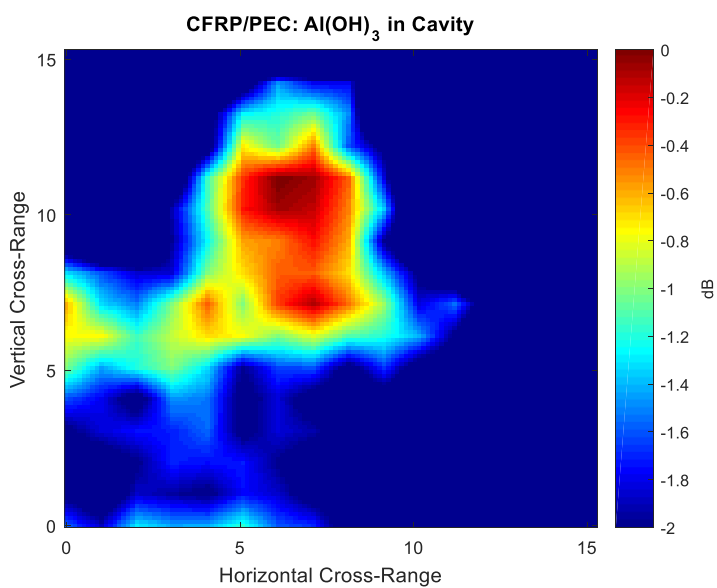
Sample:	8-ply Unidirectional CFRP/Aluminum hybrid composite
Scenario	Simulated Galvanic Corrosion ($Al(OH)_3$)
Waveforms tested	Noise Pulse
Standoff Distance	$R_0 = 12$ cm
Scan Dimensions	20.32cm \times 20.32 cm
Cross-range sampling interval (both vertical and horizontal)	1.016 cm

It must be noted that the two images were normalized based on the maximum return from the case of the $Al(OH)_3$ present in the cavity. This way, the results are based on the same relative scale. Here we see that for the *without* $Al(OH)_3$ case the total reflections are approximately 1-dB lower than in the *with* $Al(OH)_3$ case. Although the differences are minor, these results suggest that even while a CFRP panel is backed by a PEC sheet, the variations due to galvanic corrosion are still detectable.

A limitation of this approach lies in the fact that a unidirectional CFRP sample was used. If the sample were a quasi-isotropic sample, it is expected that the EM waves would not penetrate the sample and the detection of the $Al(OH)_3$ would be unachievable, unless galvanic corrosion had occurred at locations of rivets, bolts, etc.



(a)



(b)

Figure 5-19: Scan results of CFRP/aluminum hybrid sample (a) without the presence of Al(OH)₃ and (b) with Al(OH)₃ present.

5.3.3 Impact Damaged CFRP Sample

As mentioned in Chapter 1, damages include impacts by hailstones, birds, and handheld tools. It is then a necessity to determine whether small degrees of damage have occurred within the inner structures of these materials in a more efficient manner than through the broadly used visual inspection techniques.

In this section we present the test case where a common place tool, a hammer (Figure 5-20), is used as a device to inflict impact damage onto a 8-ply unidirectional CFRP panel shown in Figure 5-21a. The hammer weight is 0.652 kg and was dropped from a height of 1.09 m, leading to an impact energy of approximately 7.00 J—to be noted, the hammer was dropped with the head facing downwards along the orientation of the fibers. The impact caused a minor visible surface crack, which is shown in Figure 5-21b. Testing parameters are shown in table 5-6.

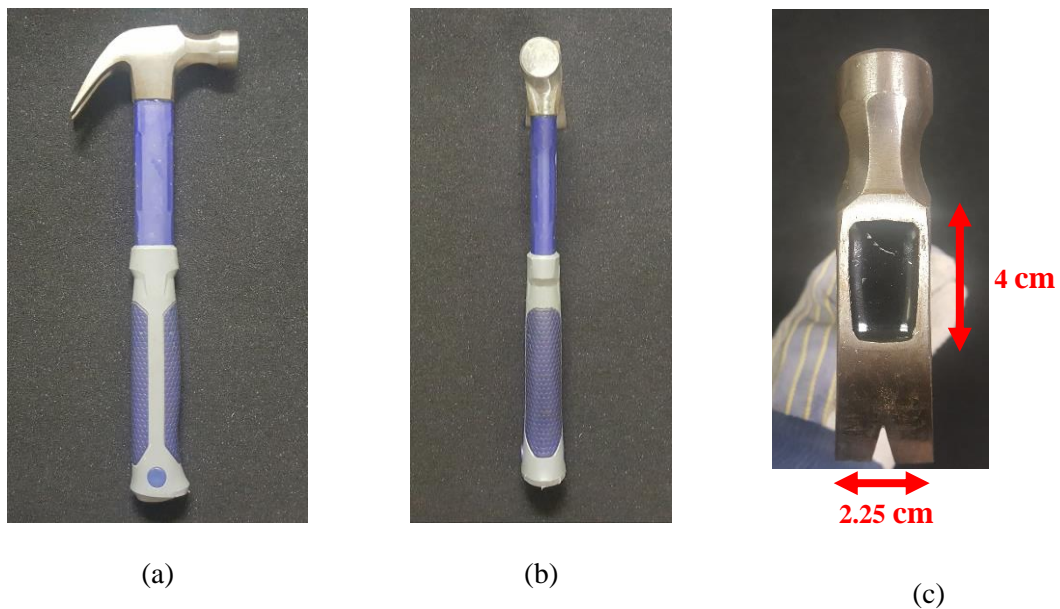


Figure 5-20: Hammer used from impact damage testing of CFRP panel. (a) side-view (b) face-view (c) hammer head dimensions.

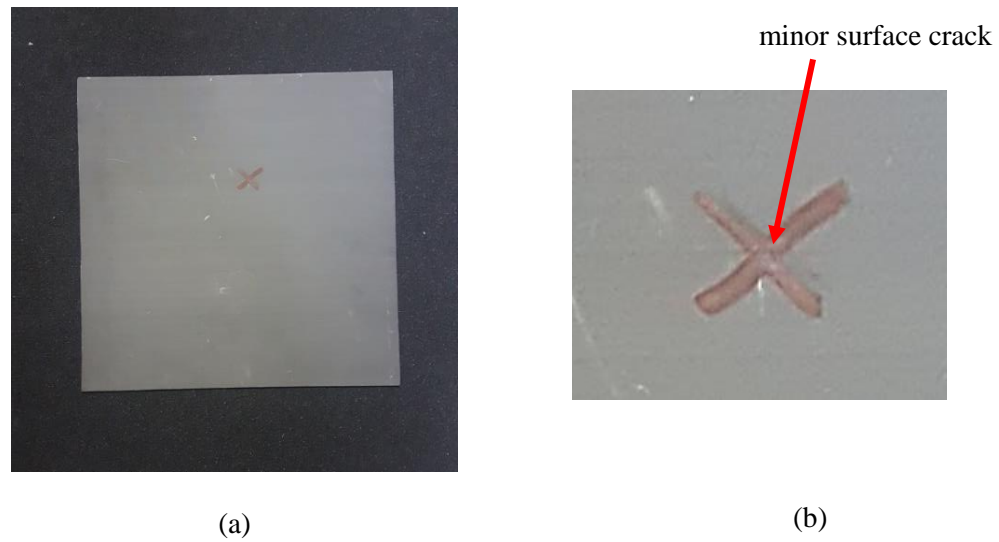


Figure 5-21: (a) CFRP panel with impact damage from hammer. Location of impact denoted by “X”. (b) Close-up of location of impact, showing minor surface cracking.

Table 5-6: Testing Parameters for CFRP Composite with Impact Damage	
Sample:	8-ply Unidirectional CFRP (No loading)
Scenario	Impact Damage from hand tool (hammer)
Waveforms tested	Noise Pulse
Standoff Distance	$R_0 = 12$ cm
Scan Dimensions	10.16 cm \times 10.16 cm
Cross-range sampling interval (both vertical and horizontal)	0.508 cm

The results of the scan are shown in Figure 5-22. The results show that extensive fiber breakage occurred at locations removed from the actual point of impact. If the reconstructed image

is compared to the image of the hammer head in 5-20c, it is possible to match the dimension to the area of inflicted damage determined by the C-scan.

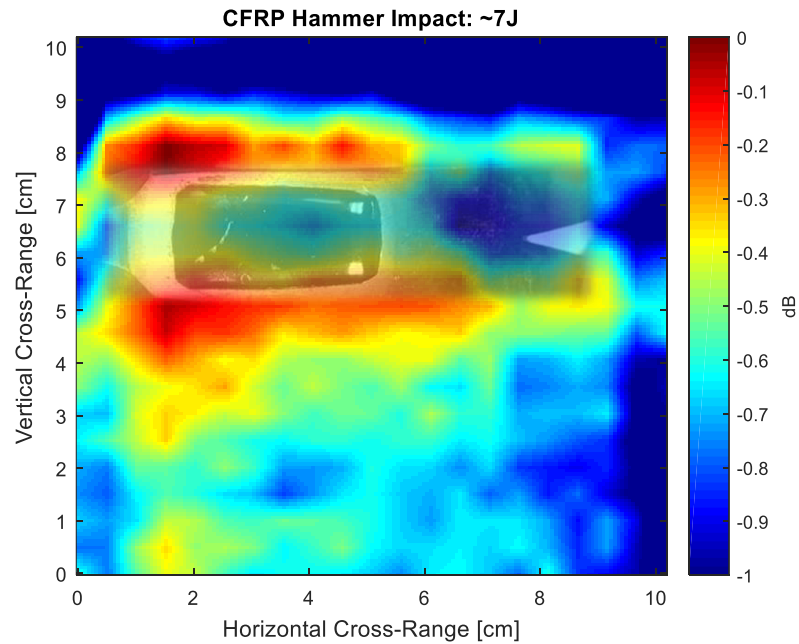


Figure 5-22: C-scan results of impact damage due to hammer drop on CFRP composite sample.

It should be noted that successful capture of the internal fiber damage is heavily dependent of reduction of the influence of stand-off distance non-uniformity. Previous tests proved unsuccessful due to variations in the standoff distances between the antennas and the sample at the four corners of the sample. To be able to neglect this errors, the standoff distance variations needed to be less than 1 mm difference at each extent of the scanning dimensions. Alternatively, and assuming a high sample rate, these effects may be compensated for in post-processing by measuring the variance in index value of the reflection from the front surface of the sample, or by using multiple antenna polarizations, as in [7].

Chapter 6 Conclusion and Suggestions for Future Work

6.1 Conclusions

This thesis discussed a nondestructive testing (NDT) approach based on microwave imaging using ultrawideband (UWB) noise pulses. The main area of focus was in detecting the presence of delaminations due to impact damages and the effects of galvanic corrosion in composite materials. The main composite samples of focus were carbon-fiber reinforced polymers and glass-fiber reinforced polymers. Tests were conducted to see if the microwave NDT approach using UWB noise pulses were capable of detecting such flaws, which based on our work, suggests that the use of noise pulses for NDT has benefits over alternative waveforms and other forms of NDT. Using these types of noise pulses we were able to detect the presence of air voids in GFRP reinforced cement walls, detect the byproduct of galvanic corrosion in hybrid CFRP/aluminum samples, and detect/localize impact damages on a 8-ply unidirectional CFRP sample.

A study into the effectiveness of the noise pulses was also conducted to identify how well they identify boundaries within multilayered dielectric materials. What our findings suggest is that optimal noise pulses for NDT must be tailored for the application to reduce target masking due time-domain sidelobes. Due to the random fluctuations of the noise signals, any given iteration may cause high peak-to-sidelobe ratios in the output of its autocorrelation function. Hence a method of identifying noise waveforms with low peak-to-sidelobe ratios is necessary for accurately sensing multiple layers in a material.

A NDT microwave imaging system was designed to conduct tests in the X-band frequency region. The development of the hardware was discussed and demonstrated through a series of simulations of target ranging experiments.

6.2 Future Work

There proves to be room to expand the abilities of the system in detecting impact damages in other scenarios, such as with a degree of loading on the composite material. Many times in actual cases, composites are under load, such as when an aircraft is in the air versus on the ground. Also, in the case of CFRP, when the cause of the impact damages is in a different orientation from that of the internal fiber structure may yield different breakage patterns. Further work would also benefit from learning the degree to which microwave imaging may be applied to the cases of quasi-isotropic composite materials.

More work may be done in developing a robust method of assuring optimal noise waveforms for imaging. Also, further insight into the effects of the variances of the time-bandwidth produce with regard to peak-to-sidelobe and integrated sidelobe levels may prove beneficial.

Future investigations may benefit working with other types of composite materials, such as carbon nanotube reinforced polymers which have increasing interest in many military applications.

References

- [1] R. Zoughi, *Microwave Non-Destructive Testing and Evaluation*, Dordrecht: Kluwer Academic Publishers, 2000.
- [2] "NDT Resource Center," [Online]. Available: <https://www.nde-ed.org/AboutNDT/SelectedApplications/AircraftInspection/Aircraft%20Inspection.htm>. [Accessed May 2018].
- [3] "The American Society For Nondestructive Testing," 2017. [Online]. Available: https://www.asnt.org/MajorSiteSections/Certification/ASNT_NDT_Level_III/Examinations/VT.aspx. [Accessed May 2018].
- [4] B. Zonnefeld and R. Zoughi, "Permittivity characteristics of Kevlar, carbon composites, E-glass, and rubber (33% carbon) at X-band (8–12 GHz)," *Review of Progress in Quantitative Nondestructive Evaluation*, vol. 10B, pp. 1431-1436, 1991.
- [5] "Composites Manufacturing," July 2017. [Online]. Available: <http://compositesmanufacturingmagazine.com/2017/07/airbus-delivers-100th-a350-xwb/>. [Accessed May 2018].
- [6] Z. Li, A. Soutis, A. Haigh, R. Sloan and A. Gibson, "Application of an electromagnetic sensor for detection of impact damage in aircraft composites," *2016 21st International Conference on Microwave, Radar, and Wireless Communications (MIKON)*, pp. 1-4, 2016.
- [7] S. Kharkovsky, A.C. Ryley, V. Stephen and R. Zoughi, "Dual-Polarized Microwave Near-Field Reflectometer for Non-Invasive Inspection of Carbon Fiber Reinforced Polymer (CFRP) Strengthened Structures," in *2006 IEEE Instrumentation and Measurement Technology Conference Proceedings*, Sorrento, 2006.

- [8] R. Sutthaweekul, A. M. J. Marindra and G. Y. Tian, "Study of microwave responses on layered woven CFRP composites," in *2017 9th International Conference on Information Technology and Electrical Engineering (ICITEE)*, Phuket, 2017.
- [9] S. Heimbs, S. Heller, P. Middendorf, F. Hähnel and J. Weiße, "Low velocity impact on CFRP plates with compressive preload: Test and modelling," *International Journal of Impact Engineering*, vol. Volume 36, no. Issues 10–11, 2009.
- [10] M. McElroy, W. Jackson, R. Olsson, P. Hellström, S. Tsampas and M. Pankow, "Interaction of delaminations and matrix cracks in a CFRP plate, Part I: A test method for model validation," *Composites Part A: Applied Science and Manufacturing*, vol. 103, pp. 314-326, 2017.
- [11] R. James, *Prognostic Investigation of Environmentally Assisted Damage in Aerospace Composite Materials and its Detection Strategy*, University Park: The Pennsylvania State University, 2017.
- [12] Y. H. Kim, Y. D. Jo, S. Y. Bae and S. J. Sin, "Material design of Al/CFRP hybrid composites for the hull of autonomous underwater vehicle," in *OCEANS 2010 IEEE - Sydney*, Sydney, 2010.
- [13] "Nace International," 2018. [Online]. Available: <https://www.nace.org/Pitting-Corrosion/>. [Accessed May 2018].
- [14] E. Hakansson, *Galvanic Corrosion of Aluminum/Carbon Composite Systems*, 2016.
- [15] J. Liang, Q. Liang, S. W. Samn and R. M. Narayanan, "Sense-Through-Wall Channel Modeling Using UWB Noise Radar," in *2009 IEEE Globecom Workshops*, Honolulu, HI, 2009.

- [16] P. H. Chen, M. C. Shastry, C. P. Lai and R. M. Narayanan, "A Portable Real-Time Digital Noise Radar System for Through-the-Wall Imaging," *IEEE Transactions on Geoscience and Remote Sensing*, vol. 50, no. 10, pp. 4123-4134, Oct 2012.
- [17] R. M. Narayanan, "Through wall radar imaging using UWB noise waveforms," in *2008 IEEE International Conference on Acoustics, Speech and Signal Processing*, Las Vegas, NV, 2008.
- [18] X. Dong, Y. Zhang and W. Zhai, "A sparse optimization method for masking effect removal in noise synthetic aperture radar," in *2016 IEEE International Geoscience and Remote Sensing Symposium (IGARSS)*, Beijing, 2016.
- [19] R. M. Narayanan and N. S. McCoy, "Delayed and summed adaptive noise waveforms for target matched radar detection," in *2013 22nd International Conference on Noise and Fluctuations (ICNF)*, Montpellier, 2013.
- [20] R. Vela, R. M. Narayanan, K. A. Gallagher and M. Rangaswamy, "Noise radar tomography," in *2012 IEEE Radar Conference*, Atlanta, GA, 2012.
- [21] R. Bourret, "A Proposed Technique for the Improvement of Range Determination with Noise Radar," *Proc. IRE*, vol. 45, no. 12, pp. 1744-1744, 1957.
- [22] B. Horton, "Noise-Modulated Distance Measuring Systems," *Proc. IRE*, vol. 47, no. 5, pp. 821-828, May 1959.
- [23] M. Z. Win, D. Dardari, A.F. Molisch, W. Wiesbeck and J. Zhang, "History and applications of UWB [Scanning the issue]," *Proceedings of the IEEE*, vol. 97, no. 2, pp. 198-204, 2009.
- [24] R. Narayanan, "Through-wall radar imaging using UWB noise waveforms," *J. Franklin Institute*, vol. 345, no. 6, pp. 659-678, Sept 2008.
- [25] M. G. Amin, *Through-the-Wall Radar Imaging*, Boca Raton, FL: CRC Press, 2011.

- [26] C. Balanis, *Advanced Engineering Electromagnetics*, Hoboken, NJ: John Wiley and Sons, 2012.
- [27] A. Barasinski, H. Tertrais, C. Ghnatios and F. Chinesta, "Processing of a carbon fiber reinforced polymer (CFRP) laminate part by microwaves," in *2016 IEEE Conference on Electromagnetic Field Computation (CEFC)*, Miami, FL, 2016.
- [28] D. Jenn, "Radar Fundamentals," [Online]. Available: <http://faculty.nps.edu/jenn/Seminars/RadarFundamentals.pdf>.
- [29] "Assesing and Improving Radar System Performance: Application Note Part 7," Keysight Technologies, 2017. [Online]. Available: <http://literature.cdn.keysight.com/litweb/pdf/5992-2155EN.pdf>.
- [30] K. Kulpa, *Signal Processing in Noise Waveform Radar*, Norwood, MA: Artech House, 2013.
- [31] C.-P. Lai, *Through Wall Surveillance Using Ultrawideband Random Noise Radar*, 2007.
- [32] S. K. Mitra, *Digital Signal Processing: A Computer-Based Approach*, New York, NY: McGraw-Hill, 2011.
- [33] A. Z. Liu, R. M. Narayanan and M. Rangaswamy, "Information elasticity in pseudorandom code pulse compression," in *Proc. SPIE 10633, Radar Sensor Technology XXII*, Orlando, FL, 2018.
- [34] P. G. Singerman, R. M. Narayanan and M. Rangaswamy, "Information elasticity in ultra-wideband target detection amongst distributed clutter," in *Proc. SPIE 10633, Radar Sensor Technology XXII*, Orlando, FL, 2018.
- [35] J. A. LaComb, P. M. Mileski and R. F. Ingram, "Ultra wideband surface wave communication," *Progress in Electromagnetics Research C*, vol. 8, pp. 95-105, 2009.

- [36] R. M. Howard, "White noise: A time domain basis," in *2015 International Conference on Noise and Fluctuations (ICNF)*, Xian, 2015.
- [37] K. Lukin and P. Vyplavin, "Integrated sidelobe ratio in noise radar receiver," in *2012 13th International Radar Symposium*, Warsaw, 2012.
- [38] H. Haghshenas and M. M. Nayebi, "Online low-sidelobe waveform generator for noise radars based on the graph theory," *IET Radar, Sonar & Navigation*, vol. 7, no. 1, pp. 75-86, 2013.
- [39] A. Richards, *Fundamentals of Radar Signal Processing*, New York: McGraw-Hill Education, 2014.
- [40] T. Fritz and M. Eineder, "TerraSAR-X Ground Segment: Basic Product Specification Document," 2008.
- [41] D. M. Pozar, *Microwave Engineering*, Hoboken, NJ: John Wiley and Sons, 2012.
- [42] M. Steer, *Microwave and RF Design*, Edison, NJ: SciTech Publishing, 2013.
- [43] "Mini-Circuits: Amplifier Terms Defined," 2015. [Online]. Available: <https://www.minicircuits.com/app/AN60-038.pdf>.
- [44] W. Bao, Y. Yang and Tongyi, "Pyramid horn-a near field sensor for NDT," in *2000 2nd International Conference on Microwave and Millimeter Wave Technology Proceedings*, Beijing, 2000.
- [45] "Occupational Safety and Health Administration," United States Department of Labor, 1990. [Online]. Available: https://www.osha.gov/SLTC/radiofrequencyradiation/electromagnetic_fieldmemo/electromagnetic.html#section_.

- [46] "Field Regions," Antenna-Theory, [Online]. Available: <http://www.antenna-theory.com/basics/fieldRegions.php>. [Accessed 2018].
- [47] "Technical Data Sheet: ML-10050," ARC Technologies, June 2017. [Online]. Available: <http://arc-tech.com/pdf/ML-10050%20Rev%20D.pdf>.
- [48] S. Kharkivsky, A. C. Ryley, V. Stephen and R. Zoughi, "Dual-Polarized Near-Field Microwave Reflectometer for Noninvasive Inspection of Carbon Fiber Reinforced Polymer-Strengthened Structures," *IEEE Transactions on Instrumentation and Measurement*, vol. 57, no. 1, pp. 168-175, 2008.

Appendix A

CFRP Sample Preparation and Safety Procedures

To prepare such samples, one must exercise caution while working with materials that create micro fiber dust that is created while cutting, drilling, or sanding such materials. If these dust fibers come in contact with bare skin or one's eyes, the results will be pain and itching in the affected area. General information regarding working with these materials are as follows:

- Prevent generating plumage, dust, and fly by frequently dusting
- Never try rubbing edges of FRP, as micro fibers can easily penetrate deeply into the skin causing secondary inflammations
- Always wear goggles and gloves
- Always wear a mask, as particles that enter the lungs will attack mucous membranes
- High speed cutting creates toxic dusts
- Dust from CFRP is conductive and may cause electrical short circuits

What to do in the event of an exposure

- Exposure to skin
 - Use cold water and soap (do not use warm water as it will open pores and make it easier to dust fibers to enter the skin)
 - Anticipate effects of contact (itching/pain) for at least half a day
- Exposure to Eyes
 - Wash eyes with cold water for a minimum or 15 minutes
 - Contact doctor immediately
- Exposure to throat

- Wash out mouth with clean air
- Swallow large quantities of water and then induce vomiting

Cutting and Sanding CFRP

- Due to hazards associated with working with CFRP, spending more time measuring/aligning cuts is beneficial to avoid having to make additional cuts
- Use relief cuts when cutting long sections
 - Sections will fall off and stay out of the way
- Do not use blades with jagged teeth
 - Best to use blades with abrasive edges
 - Tungsten Carbide grit-style blades work the best
- Using a Hacksaw
 - Cut slightly wide of cut, then sand down using a sanding block
 - Again, use abrasive cutting blade
- Using a Dremel
 - Most “professional” technique
 - Use abrasive cutting wheel such as diamond wheel
- Using a Rodsaw
 - First create hole using metal working drill bit
- Using Angle Grinder
 - Works very quickly
 - Due to high speed, this technique generates high amounts of dust so use of a sophisticated mask is necessary
- Using a Jigsaw
 - Gritted blade (no teeth) – Least amount (if any) cracking

- Metal blade - some cracking
- Wood blade – excessive cracking, do not use
- Sanding CFRP
 - Use Permabrit block
 - Sanding block wrapped with paper
 - 120 grit wet/dry
 - 240 for finishing
 - Traditional metal sanders

Appendix B

Transducer Gain

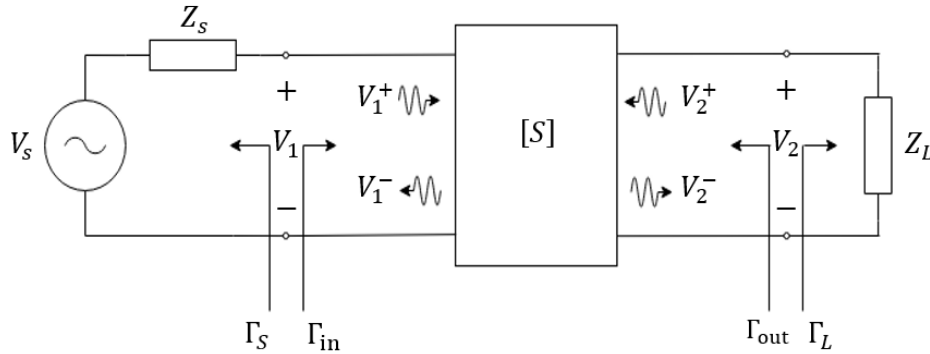


Figure B.1: Two-port system representation

For the 2-Port case, the scattering matrix takes the form

$$[S] = \begin{bmatrix} S_{11} & S_{12} \\ S_{21} & S_{22} \end{bmatrix} \quad (B.1)$$

With reference to Figure B.1 the reflection coefficient looking towards the source is given by

$$\Gamma_s = \frac{Z_s - Z_0}{Z_s + Z_0} \quad (B.2)$$

And similarly the reflection coefficient looking towards the load is

$$\Gamma_L = \frac{Z_L - Z_0}{Z_L + Z_0} \quad (B.3)$$

The input and output reflection coefficients looking into and out of the network are relating to the reflected voltages and scattering parameters by

$$\Gamma_{in} = \frac{V_1^-}{V_1^+} = S_{11} + \frac{S_{12}S_{21}\Gamma_L}{1 - S_{22}\Gamma_L} \quad (B.4)$$

and

$$\Gamma_{out} = \frac{V_2^-}{V_2^+} = S_{22} + \frac{S_{12}S_{21}\Gamma_S}{1 - S_{22}\Gamma_S} \quad (B.5)$$

Now using the expressions for the reflection coefficients and the measurable scattering parameters of the network, the following gain metrics may be determined:

- *Available Power Gain*: Ratio of the power available from the output to that of the power available from the source, given by

$$G_A \equiv \frac{P_{avo}}{P_{avs}} = \frac{|S_{21}|^2(1 - |\Gamma_S|^2)}{|1 - S_{11}\Gamma_S|^2(1 - |\Gamma_{out}|^2)} 10 \log_{10}(|P_{avo}|) - 10 \log_{10}(|P_{avs}|) \quad (B.6)$$

- *Transducer Power Gain*: Ratio of power delivered to the load to that of the power available from the source, given by

$$G_T \equiv \frac{P_L}{P_{avs}} = \frac{|S_{21}|^2(1 - |\Gamma_S|^2)(1 - |\Gamma_L|^2)}{|1 - \Gamma_S\Gamma_{in}|^2|1 - S_{22}\Gamma_L|^2} = 10 \log_{10}(|P_L|) - 10 \log_{10}(|P_{avs}|) \quad (B.7)$$

In the cases where the source reflection coefficient and the load reflection coefficient are both equal to zero, that is, $\Gamma_S = \Gamma_L = 0$, then (equation for transducer power gain) simplifies to

$$G_T = |S_{21}|^2 \quad (B.8)$$

Appendix C

FIR Filters

The time-domain representation of the Direct-Form (multiplier coefficients are the same as the transfer function coefficients) FIR filter are given by

$$y[n] = \sum_{k=0}^N h[k]x[n-k] \quad (C.1)$$

where $x[n]$ is the discrete time input sequence and $h[n]$ corresponds to the coefficients of the filter.

The outputs, $y_{1-3}[n]$, are dependent on the magnitude function, $|H(e^{j\omega})|$, of the filter and phase difference—relative to input signal $x[n]$ —given by the phase function $\theta(\omega_0) = \arg\{H(e^{j\omega_0})\}$. For many cases the magnitude function may be held at a constant value.

If the input to the filter was a single sinusoidal signal, then the output of the filter will also be of a sinusoidal nature—but lagging the input signal by $\theta(\omega_0)$ radians. This results in a *phase delay* defined as

$$\tau(\omega_0) = -\frac{\theta(\omega_0)}{\omega_0} \quad (C.2)$$

When a signal is composed of multiple sinusoidal waveforms, the phase delays for each frequency will be different when processed by a LTI discrete-time system. This is noted as the *group delay*, given as

$$\tau_g(\omega) = -\frac{d\theta(\omega)}{d\omega} \quad (C.3)$$

Where the phase function, $\theta(\omega_0)$, is assumed to be unwrapped so that its derivative exists. The unwrapped phase is used when the range is outside of $[-\pi, \pi]$ to remove unwanted discontinuities at 2π .

The derivative of the phase function is given by

$$\frac{d\theta(\omega)}{d\omega} = \frac{1}{|H(e^{j\omega})|^2} \left[H_{re}(e^{j\omega}) \frac{dH_{im}(e^{j\omega})}{d\omega} - H_{im}(e^{j\omega}) \frac{dH_{re}(e^{j\omega})}{d\omega} \right] \quad (C.4)$$

Which then allows us to define the unwrapped phase function by its derivative as

$$\theta(\omega) = \int_0^\omega \left[\frac{d\theta(\eta)}{d\eta} \right] d\eta, \quad (C.5)$$

with the constraint

$$\theta(0) = 0 \quad (C.6)$$

Using the above equations, the continuous unwrapped phase function of $H(e^{j\omega})$ may be determined. This may also be determined using *unwrap* function within MATLAB.

Such a linear phase FIR filter may be seen in Figure C.1

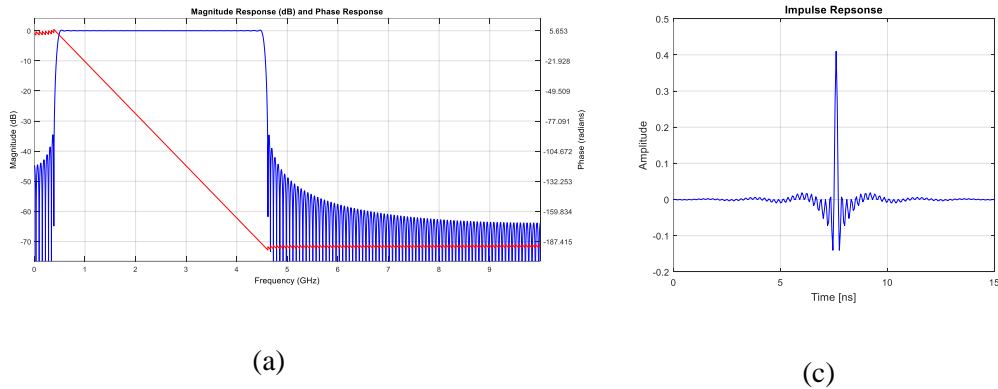


Figure C.1: (a) Magnitude and phase of FIR filter (b) Impulse response of filter